Scaling properties of temperature spectra and heat flux cospectra in the surface friction layer beneath an unstable outer layer

Johannes Laubach · Keith G. McNaughton

Submitted to Boundary-Layer Meteorology 16 October 2008

Revised Version of 11 August 2009

Johannes Laubach

Manaaki Whenua – Landcare Research, P.O. Box 40, Lincoln 7640, New Zealand

Tel.: +64-3-321 9999

Fax: +64-3-321 9998

email: LaubachJ@LandcareResearch.co.nz

Keith G. McNaughton

School of GeoSciences, University of Edinburgh, Edinburgh EH9 3JU, Scotland

Present address: *31 Paretu Drive, RD 1, Kerikeri 0294, New Zealand*

email: Keith@McNaughty.com

Abstract

Temperature variance and temperature power spectra in the unstable surface layer have always presented a problem to the standard Monin-Obukhov similarity model. Recently that problem has intensified with the demonstration by Smedman et al. (2007, Quart. J. Roy. Meteorol. Soc. 133: 37-51) that temperature spectra and heat flux cospectra can have two distinct peaks in slightly unstable conditions, and by McNaughton et al. (2007, Nonlin. Processes Geophys. 14: 257-271) who showed that the wavenumber of the peak of temperature spectra in a convective boundary layer (CBL), closely above the surface friction layer (SFL), can be sensitive to CBL depth, z_i. Neither the two-peak form at slight instability nor the dependence of peak position on z_i at large instability is compatible with the Monin-Obukhov model.

Here we examine the properties of temperature spectra and heat flux cospectra from between these extremes, i.e. from within unstable SFLs, in two experiments. The analysis is based on McNaughton's model of the turbulence structure in the SFL. According to this model, heat is transported through most of the SFL by sheet plumes, created by the action of impinging outer eddies. The smallest and most effective of these outer eddies have sizes which scale on SFL depth, z_s. The z_s-scale eddies and plumes are organised within the overall convection pattern in the CBL, and in turn they organise the motion of smaller eddies within the SFL, whose sizes scale on height, z.

The main experimental results are: 1) The peak amplitudes of the temperature spectra in the SFL are collapsed with a scaling factor $(z_s\, z)^{1/3}\, \varepsilon_o{}^{2/3}$ divided by the square of the surface temperature flux, where ε_o is the dissipation rate of turbulent energy in the outer CBL (above the SFL). 2) The peak wavenumbers of the temperature spectra are collapsed with the mixed length scale $(z_i\, z_s)^{1/2}$. 3) The peak wavenumbers of the heat flux cospectra are collapsed with the doubly-mixed length scale $(z_i\, z_s)^{1/4}\, z^{1/2}$. 4) For $z/z_s < 0.03$, the peak in the cospectrum is replaced by another peak at a wavenumber about a magnitude larger. This peak's position scales on z. 5) All these findings are consistent with the observations of Smedman et al. (2007).

Keywords: Coherent structures, Convective boundary layer, Heat transport, Impinging eddies, Temperature spectra, Unstable surface layer

1 Introduction

The "Kansas" experiment (Kaimal et al. 1972) and the "Minnesota" experiment (Kaimal et al. 1976) have an established place in the history of micrometeorology. The results from these experiments, interpreted within the framework provided by the Monin-Obukhov and Deardorff similarity schemes, have become the standard description of the atmospheric surface layer and the convective boundary layer (CBL). Even so, the temperature spectra from the Kansas experiment for the *unstable* surface layer, i.e. the surface layer beneath a CBL, were a direct challenge to the concepts that underlie the Monin-Obukhov theory. Thus Kaimal et al. (1972), henceforth KWIC72, noted that as the Monin-Obukhov similarity parameter z/L (where z is height above ground and L is the Obukhov length) changed smoothly through dawn, the peak of the temperature spectrum moved discontinuously. In stable stratification around dawn, which is to say as $z/L \rightarrow 0^+$ (where "0^+" means approaching 0 from positive values), the peak moved smoothly to lower frequencies, but as z/L passed through zero to negative values, the peak's position jumped down by a decade (KWIC72, p. 571 and Fig. 18). Then, as the day progressed and conditions became more unstable, the peak moved smoothly back to higher frequencies. This behaviour is certainly counterintuitive when placed in the context of a model whose underlying concept is of local eddies, whose form and velocity scale depend on the local shear and buoyancy flux (Obukhov 1946), both of which change continuously as the heat flux and shear stress change through neutral. The peak shifts were carefully recorded by KWIC72, but have received no further attention since. Recently two papers have described other features of temperature spectra from unstable conditions that also challenge the Monin-Obukhov interpretation of temperature spectra.

The first of these papers is by Smedman et al. (2007), henceforth SHHS07. They reported premultiplied temperature spectra, measured over both land and sea, with conditions ranging from slightly unstable with $L \approx -400$ m to moderately unstable with $L \approx -10$ m. In the range from $L \approx -150$ m to -40 m, they observed spectra with two distinct peaks, not just one as expected from the Kansas results (SHHS07 Fig. 7). One peak was at a scaled frequency $f \approx 0.3$ ($f = n\,z/u$ where n is observed frequency and u is mean wind speed at height z), a factor 4 or 5 higher than the peak at $z/L = 0^+$ from Kansas (i.e. the peak at neutral stability approached from the stable side). The other peak was at about $f \approx 0.01$. As conditions became more unstable ($L \approx -10$ m) the latter peak shifted to higher frequencies. The peak at higher frequency meanwhile diminished in power while its frequency remained approximately constant so the

lower-frequency peak came to dominate in moderately unstable conditions, with $z/L \approx -1$. Similar behaviour was noted in the *w*-*T* cospectra (where *w* stands for vertical wind speed and *T* for temperature). In the other direction, approaching neutral stratification from the unstable side, SHHS07 (Figs. 7 to 9) found that the lower-frequency peak disappeared and the peak at $f \approx 0.3$ became dominant. To account for these results, SHHS07 propose that heat is transported both by longitudinal rolls whose height spans the whole CBL and by smaller-scale eddies that impinge onto the surface and create smaller-scale turbulence.

The second paper challenging the Monin-Obukhov interpretation of *T* spectra is by McNaughton et al. (2007), henceforth MCM07. They reported spectra for very unstable conditions, with $L > -2$ m and $z/L < -0.73$ at their lowest level, over a very smooth and extensive playa surface. MCM07 observed temperature spectra with single peaks like KWIC72 and SHHS07 for very unstable conditions but, unlike those authors, they found that in order to collapse the spectral peaks on the wavenumber (κ) axis, the mixed length scale $z_i^{1/2} z^{1/2}$ was needed, where z_i is the depth of the CBL. To collapse the large-wavenumber end of the spectra they needed to scale the κ axis using $z_i^{1/4} z^{3/4}$. The appearance of z_i in these scales is in direct contradiction to the Monin-Obukhov premise that only local parameters are needed to scale local processes. It is likely that the unresolved (stippled) region in Fig. 9 of KWIC72 reflects, at least in part, an incorrect scaling of their spectra.

The purpose of this paper is to present some of our own spectral observations made in the surface friction layer (SFL), in conditions ranging from weakly to moderately unstable, and to interpret these new results by extending the structural model of MCM07 down into the SFL. The term "SFL" denotes the layer of the atmosphere in contact with the ground in which the surface drag is an important scaling parameter for velocity spectra. We use SFL to denote the layer of the atmosphere in contact with the ground in which the surface drag is an important scaling parameter for velocity spectra. In Section 2 we outline the context of our model as a complex dynamical system. Section 3 contains a description of the model as it stood prior to the analysis of the present data. Section 4 explains how the scaling parameters of the model are obtained. Section 5 describes the details of the two experiments and the data processing. In Section 6 we present the new observations, show that they are compatible with the observations of KWIC72, SHHS07 and MCM07, and argue how all of the observations can be explained by the new model.

2 The CBL as a complex dynamical system

CBLs are complex dynamical systems. They are open systems, have nonlinear governing equations, many degrees of freedom and display the defining property of such systems: they are self-organising. That is to say CBLs spontaneously produce patterns of motion, the largest and most long-lived of which are the large-scale coherent structures that span CBLs. These may take the form of convective roll vortices (e.g Ferrare et al. 1991) or polygonal patterns of convection cells, which occur when shear across the CBL is small (e.g. Melfi et al. 1985). Smaller coherent structures have also been reported near the ground, though their form is less well defined (e.g. Schols et al. 1985, Katul et al. 1997, Hommema and Adrian 2003). But the idea of "patterns of motion" goes beyond just coherent structures. Complex dynamical systems are chaotic systems that have strange attractors, and coherent structures are only the most obvious manifestation of these. Recurrent, transient features such as direct and inverse cascade processes are other examples of patterns of motion, even when their form in space and time is unknown.

As complex dynamical systems, the flows in CBLs are related to the flows in Rayleigh-Bénard cells (e.g. Bodenschatz et al., 2000): cells with convection between a heated lower plate and a cooled upper plate. Much can be learned from such systems, but the flow in a typical, horizontally uniform CBL is characterised by a much higher Rayleigh number ($\sim 10^{18}$) and the complicating effects of horizontal pressure gradients and an open upper boundary. Thus the energy required to maintain the turbulence in CBLs has three sources: the free atmosphere above, from where kinetic energy is delivered by entrainment through the capping inversion as the CBL grows during the daytime, the sun, which warms the ground and so delivers gravitational potential energy to the air in contact with the ground, and the synoptic pressure gradients acting within the CBL to create kinetic energy. There is remarkably little information on the relative importance of these three sources but, whatever the case, the combination of very large Rayleigh numbers and several sources of turbulence energy make CBL flows substantially different to the Rayleigh-Bénard flows seen in laboratory studies. This, plus the importance of CBLs in practical meteorology, are sufficient to make the study of CBLs a field of research in its own right.

A new label for turbulence in CBLs is not, in itself, very important. What is important is the perspective it gives on how turbulence in CBLs works. For this we appeal to some general properties of complex dynamical systems. Firstly, the "patterns of motion", or more generally the strange attractors of complex systems, cannot be

deduced from the governing equations by any known mathematical techniques. Instead, to predict system behaviour the governing equations must be directly integrated through time, and the patterns then deduced empirically. For CBLs the Navier-Stokes equations must be integrated either naturally in a real flow or digitally in a well-constructed computer simulation and the coherent structures and other patterns of motion extracted by whatever techniques are available. Experiment rather than theory is our primary source of information. Secondly, experience with such systems shows that strange attractors can be quite sensitive to small changes in the formulation of the governing equations and boundary conditions. The implication is that mathematical analyses based on simplified models or linearised equations can sometimes produce results that differ dramatically from the prototype. Therefore results of turbulence models are always suspect until checked against experiment. Thirdly, in complex systems the chains of cause and effect become circular, with each part of the system depending on (being "caused by") all other parts of the system. For example, and as we shall explain in more detail below, the small-scale motions in CBLs are caused by the larger-scale motions in the flow, while the larger-scale motions are caused by the aggregation of the small-scale motions.

The final attribute of such systems is controversial, and rapidly developing, but key to our assertion of the importance of understanding the patterns of motion as a route to understanding turbulence in CBLs. It is that there exists a thermodynamic optimisation principle that governs the form of strange attractors in complex systems. A focus of research has been the climate system in which, many argue, the weather patterns are such as to maximise entropy production (Ozawa et al. 2003, Lucarini 2009). If so, the same optimisation principle should apply to turbulence in CBLs. Thus the "patterns of motion" found in CBLs are, very likely, arranged so as to maximise the transport of heat and momentum for the given external driving (geostrophic flow and surface forcing). These patterns of motion are thus *the* central concern in understanding the transport of momentum and scalars in CBLs.

3 A structural model for heat transport in the SFL

Here we briefly review the structural model of turbulence in the lower part of the CBL developed by McNaughton (2004a, b, 2006) and MCM07 and explore its implications for heat transport within the lowest part of the CBL, the SFL. Our model is a "complex dynamical system" model, in that it is based on a description and interpretation of the

recurring patterns of motion which develop spontaneously in real CBLs. One reason for summarising past work is that our understanding has evolved while the above papers were being published. In particular, the original account of eddies within the SFL (McNaughton 2004a, b, 2006) dealt with momentum transport only, and was written before MCM07 presented their account of eddy processes immediately above the SFL. Here we reconsider turbulence processes near the ground, including the suggestion by MCM07 that scalar transport near the ground is by the action of impinging outer eddies. The model described below is as it stood before our new analysis of data from within SFLs. As one would hope, the new data and analysis have given new insights and filled in a gap in the model. The purpose of this section is to provide a platform for understanding the new developments.

3.1 Kinds of eddies

We use the term "eddy" to describe all or any part of a "pattern of motion". That is, our eddies include well-defined coherent structures and less well-defined transient patterns of motion, such as occur in cascades, or even parts of cascades. In each case the word "eddy" will indicate structured rather than random motion, but beyond that we rely on context to make our meaning clear.

Our model classifies eddies as "inner" or "outer" eddies according to their origins, and as "attached" or "detached" eddies depending on whether or not they extend down to the ground. Our categorisation of eddies as inner or outer eddies is essentially the same as Townsend's division into active and inactive motions (Townsend 1976). We prefer our terminology because, in our model, some outer eddies are decidedly active in heat transport within the SFL. Our classification of eddies as either attached or detached is also adopted from Townsend (1951, 1976). Thus, in the terminology suggested by Jiménez (1999), our model is a "Townsend model". The inner eddies are attached eddies directly created by velocity shear near the ground, together with smaller eddies created by their breakup. Inner eddies are the principal transporters of momentum within the SFL. Outer eddies, on the other hand, are associated with the large, attached, coherent structures that span the CBL and transport both heat and momentum through the bulk of the CBL, together with the smaller eddies associated with their breakup.

Though our model has its foundation in Townsend's ideas, we introduce some modifications. These are of minor importance when only velocity statistics are

considered, as in Townsend's work on momentum and energy, but they have major implications for the transport of heat and other scalars within the SFL in convective conditions. In our scheme the attached outer eddies have a greater range of sizes, with the important consequences that the smallest of them do not move quite horizontally when they impinge onto the ground, so they can transport heat, and they can interact with inner eddies when their sizes are similar. We develop these ideas below.

3.2 Outer eddies

The largest outer eddies are the coherent structures that span the CBL, whether in the form of roll vortices aligned with the wind shear or convective cells. Because they span the CBL, their characteristic height is z_i, and, since they have a characteristic form, the same length scale characterises their lengths and widths. These large eddies are attached since they extend down to the ground, and their motions are almost horizontal where $z << z_i$. Near the ground they can be detected by their contribution to the power spectra of streamwise and lateral wind components at small wavenumbers, where $\kappa z_i \sim 1$. These large eddies, though long-lasting, are not permanent: they break up continuously and pass their energy downscale to smaller, less organised eddies, which are detached. Thus the z_i-scale eddies receive their energy from sources originating outside the CBL, and they pass it on via the outer "Richardson" cascade to smaller and smaller eddies, and ultimately to dissipation as heat (Richardson 1920). This continuous flow of energy from larger to smaller structures is necessary to maintain the patterns of motion as a statistically steady state against the universal trend towards disorder (increase in entropy).

Though there are three sources of turbulence energy in CBLs, it is enough for present purposes to know that when the turbulence is statistically steady the total rate of turbulence energy delivery must equal the loss to dissipation within the CBL. Experiments show that the dissipation rate is usually constant with height above the SFL (Kaimal et al. 1976, MCM07), so dissipation in the bulk of the CBL can be characterised by a single value, called the "outer" dissipation rate, ε_o. Using the Kolmogorov law for the inertial subrange, we know the energy density associated with eddies of any particular size as $(\varepsilon_o/\kappa)^{2/3}$, where κ is the wavenumber associated with eddies of that size. An energy scale for the largest eddies can be constructed by extrapolating the inertial subrange up to the scale of the largest eddies so, to within a

fixed numerical factor, the energy density of the largest eddies can be written as $(z_i\,\varepsilon_o)^{2/3}$.

The outer inertial subrange in CBLs spreads over many decades, so there is no fixed connection between the wavelengths of eddies within the Richardson cascade and any characteristic length of the system. However, outer Richardson eddies are carried along within larger Richardson eddies, and ultimately within z_i-scale eddies, breaking up continuously as they go, and some of them are swept down into contact with the ground, thereby becoming attached. MCM07 suggest that the impinging outer eddies transform, through blocking by the ground, into pairs or arrays of streamwise roll vortices aligned with the wind. These roll vortices are of the same general shape as the z_i-scale roll vortices, but they are smaller. Attached outer eddies are particularly significant for scalar transport, since they sweep up heat from near the ground and create temperature plumes in the convergence regions between them. Though their origin lies in the length-scale-free outer Richardson cascade, attachment gives characteristic length and energy scales to the population of attached eddies. At any height z the impinging eddies with the greatest vertical velocities have heights $\sim 2\,z$, and thus wavelengths close to π/κ. Eddies of that size in the outer Richardson cascade have energies $\sim (z\,\varepsilon_o)^{2/3}$, which gives an energy scale for the outer, attached roll vortices at height z.

3.3 Inner eddies

Inner eddies are produced by the shear layer near the ground and take their energy from the larger-scale processes that maintain that shear. They are associated with the transport of momentum within the SFL. The forms of the main momentum-transporting eddies in the SFL have proven to be quite elusive, and there is, as yet, no consensus, though many authors talk of hairpin packet models (e.g. Perry and Chong 1982, Hommema and Adrian 2003). Here we adopt a version of this, the TEAL (Theodorsen Ejection-Amplifier-Like) model proposed by McNaughton (2004a, b, 2006). This is an inverse cascade model of the kind discussed by Jiménez (1999). It is "inverse" in the sense that attached eddies arise near the ground and then grow in size by a cyclic process to beget larger and larger eddies. This progression from smaller to larger is the inverse of the standard downscale progression in the Richardson cascade. Jiménez calls this a "Townsend cascade" since the eddies are attached and transport momentum. Because of these properties, eddies of the inverse cascade have lengths

which scale on z, and energies which scale on the square of the friction velocity, u_* (or its generalisation, u_ε, see next section).

In our model the TEAL structures compete for space as they grow, so the less symmetrical – the majority at each level – become distorted, cease growing and break up, whence their energy passes down to the inner Richardson cascade. Most of these inner Richardson eddies are detached but some are attached, or become attached when carried down into contact with the ground. The majority of inner Richardson eddies dissipate within the SFL, but some are carried upwards within the warm plumes swept up between the attached outer eddies to finally dissipate at greater heights (MCM07). Within the SFL this export is reflected in a normalised dissipation rate that initially decreases with height rather than increasing monotonically from the neutral value (e.g. Edson and Fairall 1998), as would be expected if the power delivered to the TEAL cascades was all dissipated locally.

3.4 Interactions between inner and outer eddies

Eddies of different kind but similar size cannot exist in the same place at the same time: one or the other must prevail. Logically there is a third possibility – that interaction produces new kinds of eddies – but this does not seem to happen. The reason may be that eddies are limited to just a few general forms so that intermediate structures cannot be anything other than briefly transitional. By far the most common class of eddies are vortex tubes, which can take many forms: horizontal tubes, as in attached roll vortices or detached quasi-streamwise vortices; vertical tubes, as in dust devils or tornadoes; tubes bent back on themselves, as in hairpin eddies; bent and rejoined, as in toroids (examples of which are the convection cells common in strongly unstable CBLs); and as tangled masses of tubes of many sizes, as found in decaying turbulence (Farge et al. 2001). Another group is our TEAL structures. They are distinct because there is no suggestion of translational symmetry along any tube axis, and because growth is a fundamental characteristic. They are necessarily attached eddies and exist only in wall-bounded shear layers. A full eddy taxonomy may include other families, but these have not been described. For the present we propose that intermediate forms do not exist because they would not be viable, self-organising structures within the context of the Navier-Stokes equations.

In our model, inner and outer eddies of similar scale meet and interact at the top of the SFL (McNaughton, 2004b). The inner eddies are attached, so at that level they

have heights comparable to the depth of the SFL, z_s. The outer eddies have a full range of sizes, being Richardson eddies formed within larger-scale outer eddies that carry them down towards the SFL. TEAL structures grow upwards from the ground into the bases of these large outer eddies when these impinge onto the ground (become attached). The resulting interaction determines both the maximum height to which the TEAL cascades can grow, and the minimum size of the outer eddies that can avoid strong interaction and so penetrate the SFL and impinge onto the ground. The average height at which this inner-outer interaction occurs, z_s, is an important parameter of our model.

Individual eddies are temporary structures, so continual regeneration is necessary if a statistically steady population is to be maintained. That requires a continuous flow of energy through the system. McNaughton (2004b) proposed that the kind of eddy that dominates at any height is the one supported by the greatest flow of energy. At each scale the population of outer Richardson eddies is renewed by the breakup of larger eddies, so the energy that maintains their population is the spectral energy flowing down the outer Richardson cascade. This energy flow is independent of scale, and experiments show it to be independent of height (on most occasions). The power delivered to the outer detached eddies of any scale is thus ε_o. In contrast, TEAL structures are powered by the shear, and so receive their energy directly from the larger-scale processes, ultimately synoptic-scale processes, that maintain that shear against the retarding effects of surface drag (McNaughton 2006). At any height z, energy is supplied at the rate $u_\varepsilon^3/(k\,z)$, where k is the von-Kármán constant. Here u_ε is the friction velocity generalised to include the effects of fluctuating wind direction (McNaughton 2006). We call u_ε the "dissipation velocity" because it is related to total production of turbulence energy and so, ultimately, to dissipation. The SFL depth, z_s, is then defined as the height where the energy flows to the interacting inner and outer eddies are equal:

$$z_s = u_\varepsilon^3/(k\,\varepsilon_o). \qquad (1)$$

3.5 Heat transport in the SFL

Heat transport in the SFL is associated with the ramp-cliff structures observed on temperature traces. Antonia et al. (1979) showed that these are the signature of large-scale (outer) eddy motions rather than a necessary local consequence of buoyancy in the plumes. (We will use the term "plume" generically to refer to elements of

temperature patterns, in much the same way that we use "eddy" to refer to elements of the patterns of motions.) The temperature statistics therefore depend on outer parameters through most of the SFL, even while the statistics of vertical velocity depend primarily on inner parameters. Momentum transport is, on the other hand, associated with inner scaling in the SFL. These differences in scaling properties led Lumley and Panofsky (1964) and Tennekes (1970) to propose that heat and momentum are carried by different kinds of eddies. This conclusion, though inescapable, remained outside mainstream thinking in micrometeorology because the dominant paradigm was statistical and local, and so not able to address the actions of different kinds of eddies. Here we describe heat transport (and momentum transport in the next section), both within the SFL and closely above, in terms of the types of eddies proposed by MCM07.

Based on observations above the SFL, MCM07 proposed that heat is transported upwards in the common-up region between pairs of attached, outer, counter-rotating, streamwise roll vortices. Heat plumes therefore appear as long thin sheets of rising warmed air, called "sheet plumes" by Puthenveettil and Arakeri (2005). It is these sheet plumes that give rise to the ramp-cliff structures that are a universal feature of temperature time series measured near the ground. First, a fast, cool eddy sweeps down and contacts the ground, creating a microfront as it displaces the air ahead (Mahrt and Howell 1994). The arrival of a microfront is marked by a sudden drop in temperature, the "cliff" of a ramp-cliff structure. The impinging eddy, now in contact with the ground, develops into an array of counter-rotating streamwise vortices that sweep up heat from near the ground and lift it upwards in a set of parallel sheet plumes. A stationary observer on the line of a plume sees the temperature rise progressively as the plume develops. Surface drag slows the impinging eddy, until it too is displaced by a new eddy sweeping in from above. The local heat flux is largest when the sheet plume is best developed, which is just before the cliff (Mason et al. 2002). Temperature is steady in the common-down regions between rolls, and an observer placed there will see a period of steady temperature following a cliff.

The starting point for our model of heat transport is therefore the proposition that impinging eddies of scales significantly larger than z_s penetrate to the ground and transport heat within the SFL. Air warmed at the ground is swept together and upwards in the common-up regions between these roll eddies, and cooler air is transported down in the common-down regions; both regions contribute to the eddy flux of heat. The heat transport is efficient because the plumes of warmer air move over

vertical distances comparable to z_s. This is possible because, due to active pressure redistribution of energy and momentum within them (Zhuang 1995), the inducing eddies maintain their shape for long periods (compared to z/u_*) against the distorting effects of drag. At the beginning of the present analysis the idea was that the smallest of these outer eddies – those just large enough to avoid strong interaction with the inner TEAL structures – must have small enough diameters that they can generate plumes with significant vertical velocities down to very small heights. Very near the ground heat transport is by the *z*-scale eddies which, because of their overwhelming energy at very small *z*, must transport heat from the ground up into the bases of the z_s-scale eddies.

Thus the hypothesis guiding the present analysis is that *z*-scale eddies carry the heat up the first little distance from the ground, to a height where it can be swept up directly by the z_s-scale outer eddies, which have sufficient vertical velocity to carry it upwards and out of the SFL, even at such small heights. Results from our analysis below, using data from within the SFL, will modify this hypothesis.

3.6 Momentum and heat transport compared

Above the SFL, roll vortices transport momentum rather inefficiently since, with their forward velocity being the same on both sides, the common-up and common-down regions transfer similar amounts of momentum, but in opposite directions. Roll eddies therefore contribute to the variability of the momentum flux more than they contribute to the flux itself. This contrasts with their efficiency in transporting heat, since cool-down and warm-up events both contribute to the flux. The transport of momentum in direction sometimes opposed to and sometimes aligned with the heat flux can be detected by wavelet coherence analysis of the heat flux and momentum flux signals: most of the heat flux is transported during brief intervals when the heat flux is either in phase (0°) or in antiphase (180°) with the momentum signal (Clement and McNaughton, unpublished results). Within the SFL, especially its lower parts, momentum is carried mostly by TEAL structures. These transport momentum much more efficiently than they transport heat. Pressure redistribution of energy and momentum within the TEAL cascades is again the key, but here it acts not to preserve a static form of the eddies but to facilitate their evolution and growth. Notably, pressure transfers energy outwards in the powerful ejections (Lin 2000) that occur in each successive stage of the TEAL cascade. Scalars are not transported by pressure

and get left behind. To scalars the motions of the TEAL structures must seem like disorganised churning. Probabilities dictate that even disorganised churning will cause some diffusion-like transport down the mean concentration gradient, but this is not efficient.

At the smallest heights the vertical velocities associated with the impinging z_s-scale eddies must approach zero while those of the inner turbulence remain constant as size decreases, so inner eddies must eventually dominate heat transport as well as momentum transport at small enough heights. Kader and Yaglom (1990) find that temperature statistics obey inner scaling within a thin layer – their dynamic sublayer – up to only $z \approx 0.04\,|L|$. Remarkably, heat transport is more efficient than momentum transport even within purely inner turbulence, the turbulent Prandtl number being about 0.85 in logarithmic layers in neutrally-stratified flows (Kays 1994, Kader and Yaglom 1990). This is significantly less than 1. To solve this conundrum we propose that, even here, heat and momentum are transported by different eddies. As above, momentum is transported principally by TEAL structures, but we extend our model of heat transport to include transport by roll eddies created by the inner Richardson cascade. These may possibly be created as attached eddies, or maybe they are carried down to impinge onto the ground. Either way, this proposal is a logical extension of the model, since it reasserts the primary importance of attached roll eddies in heat transport that was already part of our explanation for heat transport in the SFL; we simply recognise another source of energy for those eddies.

3.7 The structure of near-neutral CBLs

As (1) shows, the SFL deepens as the outer eddies become less energetic, or the inner eddies more energetic. Thus z_s and z_i may become similar in size when outer convection is weak and/or surface shear is strong. An extreme example is the hurricane boundary layer (Foster 2005). When this happens there is no room for an outer Richardson cascade to develop, so (1) becomes invalid and z_s and z_i collapse onto the common scale z_i. In a sense, the SFL grows to become the whole CBL. Calculated values of z_s that exceed a substantial fraction of z_i (say, $z_i/5$) have no physical significance for without an outer Richardson cascade there is no outer limit to the SFL.

4 Scaling parameters for the surface friction layer

The SFL depth, z_s, is defined by (1), but typical field studies do not collect all the information necessary to use this relationship directly. Measurement of ε_o would usually require sonic anemometers or fine-wire instruments mounted on a tall tower or suspended from a balloon, well above the expected height of the SFL. Direct measurement of u_ε would require a rapid-response drag plate at the ground. The latter is not always necessary because $u_\varepsilon \approx u_*$, except in near-windless convection, when the energy of the large outer eddies, $(z_i\ \varepsilon_o)^{2/3}$, is comparable to the kinetic energy of the mean flow, ${u_m}^2/2$, where u_m is the mean wind speed of the free CBL. However, a measurement of u_* by eddy correlation typically has a large sampling error, and u_ε (which it would approximate) appears in (1) to the 3rd power. To avoid these difficulties, we pursue an alternative approach to estimate ε_o, z_s and u_ε, as follows.

4.1 Outer dissipation rate

The outer dissipation rate for turbulence energy, ε_o, can be related to variables measured in the SFL, using a simplified turbulence energy budget for the whole CBL, as

$$\varepsilon_o = \psi_o\ g\ H_0/\ T \qquad (2)$$

where g is acceleration due to gravity, T mean absolute temperature, $H_0 = \overline{w'T_v'}$ the flux of virtual temperature ("buoyancy flux") at the ground, and ψ_o an empirical factor, the dimensionless dissipation rate. In the simplest possible turbulence energy budget, buoyant production is the only source and balances dissipation. If entrainment at the CBL top is completely neglected, then buoyant production decreases linearly from $g\ H_0/T$ at the ground to zero at z_i, giving an average value of $g\ H_0/(2\ T)$, hence $\psi_o = 0.5$. If it is assumed that 20 % of the buoyant production is not dissipated but instead lost by entrainment as heat flux across the CBL top, then $\psi_o = 0.4$ results. However, there may be other sources of turbulent energy in the CBL, most notably by the entrainment of kinetic energy, associated with the entrainment of momentum from aloft. It appears that there are no direct measurements of this term available to date. Instead, we rely on sparse published observations of ψ_o. Kaimal et al. (1976) found ψ_o to vary between 0.4 and 1 for different days. Other estimates of ψ_o can be retrieved from the relationship between the dimensionless dissipation rate,

$$\varphi_\varepsilon = k\ \varepsilon\ z/{u_*}^3 \qquad (3)$$

478 and $-z/L$. Kader and Yaglom (1990) published two figures of φ_ε/k vs. $-z/(k\,L)$, one
479 from their own extensive experiments, the other from a compilation of other published
480 data. For $2 < -z/(k\,L) < 100$, i.e. near and above the surface-layer top, they found a
481 linear relationship in both figures. Inserting the definition of L, one can easily see that
482 the slope equals ψ_o, i.e.

483 $$\varphi_\varepsilon = -\psi_o\, z/L \quad , \; -z/L \to \infty \tag{4}$$

484 Kader and Yaglom (1990) found $\psi_o = 1.2$ for their own data and $\psi_o = 1.1$ for the
485 compilation. Wyngaard and Coté (1971) and SHHS07 published figures of φ_ε vs. $-z/L$;
486 in either, only two data points are shown for $-z/L > 1.5$, and these points are
487 compatible with $\psi_o \approx 1.1$. Edson and Fairall (1998) reported $\psi_o = 0.99\ (\pm 0.28)$ for
488 $1.5 < -z/L < 7$, over ocean. Summarising these data, we will use $\psi_o = 1.1$ as the best
489 available approximation to obtain the *average* outer-layer dissipation rate, yet expect
490 considerable run-to-run variability around this average: ψ_o may be as low as 0.4
491 (Kaimal et al. 1976) or as high as 1.7 (average from the experiment of MCM07,
492 R. Clement, pers. comm.).

493 Combining (1) and (2) leads to

494 $$z_s = u_\varepsilon^{\,3}\, T/(\psi_o\, k\, g\, H_0) \tag{5}$$

495 Comparison of (5) to the definition of the Obukhov length, L, yields

496 $$-z_s/L = (u_\varepsilon/u_*)^3\, \psi_o^{\,-1} \tag{6}$$

497 If $u_\varepsilon = u_*$, then $-z_s/L \approx 0.9$. Given that $u_\varepsilon \geq u_*$ by definition, and allowing for the
498 variability of ψ_o, we may well round this further to

499 $$-z_s/L \approx 1 \tag{7}$$

500 where we must admit an uncertainty of order ±70 % due to the variability of ψ_o, but
501 this is good enough to position spectra fairly well on logarithmic axes, as done below.
502 The approximate equality between a key parameter of our model, z_s, and a key
503 parameter of the Monin-Obukhov model, $-L$, so begins to explain why the latter model
504 has enjoyed some empirical success even though it is based on false principles.

505

506 **4.2 Dissipation profile, SFL depth and dissipation velocity**

507 In order to retrieve z_s and u_ε properly (independent of their proxies $-L$ and u_*), one
508 needs to consider the profile of the TKE dissipation rate in the SFL, $\varepsilon(z)$. We are not

aware of any direct measurements of this profile in the unstable SFL. Instead, we use again the relationships between φ_ε and $-z/L$ (Wyngaard and Coté 1971, Kader and Yaglom 1990, Edson and Fairall 1998, SHHS07) to construct a likely dissipation profile.

Near the ground, ε varies linearly with z^{-1} (manifest as a constant line in Figs. 6 and 7 of Kader and Yaglom (1990) for $-z/(k\,L) < 0.1$, and implying that $\varphi_\varepsilon \to 1$ for $z/z_s \to 0$). Near the SFL top, ε must approach ε_o. Two necessary conditions are therefore:

$$\varepsilon_o/\varepsilon = z/z_s \quad , \; z/z_s \to 0 \tag{8a}$$

$$\varepsilon_o/\varepsilon = 1 \quad , \; z/z_s \to \infty \tag{8b}$$

In between, the previously listed references, except Wyngaard and Coté (1971), agree that there is a region in the lower third of the SFL where $\varphi_\varepsilon < 1$, with a local minimum near $-z/L \approx 0.2$ (±0.1). The existence of such a minimum is consistent with MCM07 suggesting that smaller, detached inner eddies are transported upwards within the plumes to dissipate finally at heights of up to $\approx 3\, z_s$. The minimum value is rather uncertain due to the scatter in every published dataset; 0.7 (±0.15) seems a plausible compromise. Functions that possess such a local minimum and comply with (8) can be fitted by

$$\varphi_\varepsilon = (1 - a\, z/L)^{-1} - \psi_o\, z/L \tag{9}$$

Such a shape was used by Thiermann and Grassl (1992), with $a = 3$ and $\psi_o = 1$. The parameter a determines, rather weakly, the position of the minimum (0.207 for $a = 2$, rising to 0.25 for $a = 4$, then dropping again to 0.235 for $a = 7$), and more strongly, the strength of the minimum (e.g. 0.914 for $a = 2$, 0.75 for $a = 4$, 0.613 for $a = 7$). Here we transform (9), using (4) and (8b) with (6), to

$$\frac{\varepsilon_o}{\varepsilon} = \frac{z/z_s}{\left(1 + a'\, z/z_s\right)^{-1} + z/z_s} \tag{10}$$

which obviously satisfies (8). By choosing $a' = 5$, the minimum of φ_ε is placed at $z/z_s = 0.247$, with a value of 0.694. Inverting (10) yields

$$\frac{z}{z_s} = \left(\frac{1}{a'\left(\varepsilon/\varepsilon_o - 1\right)} + \frac{1}{\left(2a'\right)^2} \right)^{1/2} - \frac{1}{2a'} \tag{11}$$

Combining (10) and (1), one obtains

$$u_\varepsilon = (k\,\varepsilon_o\,z_s)^{1/3} = \left(\frac{k\,\varepsilon\,z}{\left(1+a'\,z/z_s\right)^{-1}+z/z_s}\right)^{1/3} \qquad (12)$$

which near the ground collapses to

$$u_\varepsilon = (k\,\varepsilon\,z)^{1/3} \quad , \; z/z_s \to 0 \qquad (13)$$

Equations (12) and (13) are useful because they allow u_ε to be computed from the inertial subrange of the horizontal wind spectrum (justifying the proposed name "dissipation velocity"). Computing u_ε from ε and z is less prone to random sampling error than measuring u_*, and it is less affected by local heterogeneity and flow distortion. We emphasise that (10) to (12) represent a plausible solution in accordance with published φ_ε values, but still require direct verification by measurements of the dissipation profile.

5 Data collection and processing

The data presented here were collected in two experiments, neither originally aimed at the investigation of temperature spectra. The first, in the following referred to as the "Coorong" experiment, was designed to investigate the structure of the CBL across a change in terrain roughness (to be reported elsewhere). It yielded fewer runs than the datasets of SHHS07 or MCM07, but has the advantage that aircraft observations were available to determine z_i. The second, referred to as the "Aorangi" experiment, was designed to investigate methane emissions from beef cattle. A single sonic anemometer was operated continuously for 20 days in the same location, above extensive flat pasture land, providing 20 times as many usable runs as the Coorong experiment. No supporting CBL observations were made, so CBL depth had to be inferred from wind spectra, as described below. The Aorangi data, because of their superior sampling statistics, are considered the primary dataset to verify our proposed scaling scheme. The much smaller Coorong dataset is presented for two reasons. First, it allows direct testing of height dependence, unavailable at Aorangi. Second, it includes distinct types of CBLs spanning a larger range of z_i values than the Aorangi data.

5.1 Coorong site, setup, and aircraft operation

The Coorong experiment was conducted in October 2005. The site was 7 km inland from the Coorong coast of South Australia (35.90° south, 139.52° east). It was chosen because it featured a straight boundary between short pasture and scrubland running parallel to the coast (from north-north-west to south-south-east), so that during the afternoon the sea-breeze reliably caused the boundary to be perpendicular to the wind direction (wind blowing from the pasture to the scrub). Three sonic anemometers were set up on the pasture. One of them was an 81000V (RM Young, Traverse City, Michigan), mounted on top of a telescope mast, 7.0 m above ground. The others were CSAT-3 (Campbell Scientific, Logan, Utah), mounted on separate poles at 2.5 m height. One of the CSAT-3 was horizontally 8 m away from the RM Young, close enough to investigate the height dependence of turbulence parameters over the pasture directly. The other CSAT-3 was 450 m away to the south, to assess if the slightly different vegetation there caused a difference in roughness. This was not found to be the case, so we can treat the measurements with the two CSAT-3 as duplicates in the cross-wind direction over the same surface. A second RM Young sonic was operated in the scrub, 500 m downwind of the edge, at 7.0 m above ground. Vegetation height in the scrub was about 2.5 m. The sonic over the scrub thus operated in the roughness sublayer, not in the SFL, and for that reason will not be considered here.

The aircraft was an HK 36 TTC ECO-Dimona motorglider (Diamond Aircraft Industries, Wiener Neustadt, Austria) owned and operated by Airborne Research Australia–Flinders University, Adelaide, South Australia. It is permanently equipped with a "BAT" turbulence probe to measure pressure, all three components of air speed and temperature at 20 Hz (Hacker and Crawford 1999), as well as all necessary equipment to take out aircraft motion and calculate the wind vector in ground coordinates. The main task of the aircraft was to fly grid patterns between 10 and 100 m height above the pasture and scrub, during the afternoon, in order to collect high-frequency wind and temperature data along and across the turbulent structures in the SFL. Because of this flight pattern, it was not possible to derive ε_o from aircraft data on a regular basis. For a handful of straight aircraft runs above the SFL, ε_o was estimated from alongwind spectra. Only half of the ε_o estimates agreed with results from (2) within a factor of 2, while the others were up to a magnitude larger or smaller. We concluded that the aircraft runs were not long enough to give meaningful statistics for this purpose.

603 **5.2 Aorangi site and setup**

604 The Aorangi experiment was conducted in November 2008. The site (40.336° south,
605 175.465° east) was located on Aorangi Research Farm, ca. 20 km inland from the west
606 coast of the North Island of New Zealand, near the city of Palmerston North. The sonic
607 anemometer was an 81000V (RM Young, Traverse City, Michigan), mounted on top
608 of a telescope mast, 3.85 m above ground. The dominant wind direction (in general
609 and in this experiment) is from the west, including frequent afternoon sea breezes
610 when synoptic wind patterns are weak. On a minority of days during this experiment,
611 steady south-easterly winds associated with fine weather were encountered. The terrain
612 consisted mainly of flat paddocks. There were no significant flow obstacles to the
613 west, south and east for at least 500 m. To the north, there was a water ditch dropping
614 2 m below ground level at 40 m distance from the sonic anemometer mast, and a
615 shelterbelt at ca. 150 m distance. The paddocks immediately surrounding the sonic
616 mast had been sprayed with herbicide prior to the experiment, so that the ground was
617 initially bare; by the end, a thin cover of herbage had grown back. The bare ground
618 extended ca. 100 m from the sonic anemometer mast to the west, south and east, and
619 35 m to the north. A herd of 61 beef cattle populated the sprayed paddock to the west,
620 being fed with silage daily. The animals slightly increased the roughness length for
621 westerly flow but were otherwise irrelevant to the flow properties and heat transport.

622

623 **5.3 Sonic anemometer data**

624 All sonic anemometers were set to output data at 20 Hz. For the CSAT-3, an
625 oversampling factor of 3 was used (i.e. internally, samples were taken at 60 Hz), to
626 avoid aliasing. The oversampling error was then removed with the transfer function
627 given by Horst and Oncley (2006). The RM Young 81000V do not offer the option of
628 oversampling at 20 Hz, but since they were mounted higher than the CSAT-3 at 2.5 m,
629 aliasing would have been smaller and was thus neglected.

630 In the Coorong, measurements were taken only on days when the aircraft was
631 available, usually for between 2 and 6 h in the afternoon. The data were divided into
632 runs of 30 min duration, synchronised between sonics to 1 s precision. Data analysis
633 was restricted to wind directions between 164° and 339° relative to geographic north.
634 The fetch over uniform pasture was of order 3 km for these directions. Runs with
635 positive stability parameter L (near dusk) were excluded. During eight days of
636 measurement, there were 44 runs of acceptable wind direction when all sonics operated

simultaneously. Of these, 25 were on the four days when z_i could be determined with confidence from the aircraft data (see Section 5.5): 6, 10, 5 and 4 on 13, 14, 15 and 16 October 2005, respectively.

Characteristics of the sonic anemometers were compared in a separate experiment. Each sonic was set up on its own mast, 5.5 m apart in a straight line, 3.88 m above a flat paddock with an upwind fetch of 600 m. In this comparison experiment, running for 3 days (daytime only), the standard deviation of T differed by 3 % between CSAT-3 and RM Young, and by 1 % between sonics of the same type. Vertical temperature fluxes differed by 4 % between types and 2 % between identical sonics, respectively. u_* typically differed by 3 % on average for any pair, but with much larger scatter than for σ_T and $\overline{w'T'}$, while $(k\,\varepsilon\,z)^{1/3}$ differed only by 1 % on average, for any pair, with very little scatter. These differences were considered small enough that no retrospective corrections had to be applied to the Coorong data. Power spectra and cospectra were also compared and did not indicate any systematic differences between CSAT-3 and RM Young.

At Aorangi, measurements ran continuously from 8 to 28 November 2008, with only a handful of brief interruptions for data backup and clock resetting. A total of 1416 runs of 20 min duration were obtained. The size of the dataset allowed to determine the relationship between streamline tilt angle and wind direction. A sinusoidal pattern suggested a tilt of the instrument (incorrect levelling), leaning 1.8º off the vertical to the south-west. This finding agreed with the visual impression, *in situ* and on photographs, and therefore this tilt was removed in postprocessing by coordinate rotation. After that, a direction-independent apparent tilt of 1.3º downwards remained. This was interpreted as a flow distortion effect induced by the top-down asymmetry of the sonic probe on top of the mast, and corrected for by subtracting a corresponding fraction of the horizontal wind component from the vertical wind component, for each 20 Hz data point, before calculation of statistical moments and spectra.

5.4 Computation of spectra and SFL parameters

Power spectra for the wind components and temperature, as well as cospectra, were computed with the wavelet algorithm of Grinsted et al. (2004), based on the Morlet wavelet. We compared the wavelet-based spectra to spectra based on traditional Fourier transform and found the former slightly smoother than the latter but without

any systematic differences. The horizontal wind spectra, S_u, were used to calculate ε, via the inertial-subrange relationship

$$S_u(\kappa) = \alpha\, \varepsilon^{2/3}\, \kappa^{-5/3} \qquad (14)$$

where $\alpha = 0.5$ is the Kolmogorov constant (Sreenivasan 1995). The temperature flux measured by sonic anemometry was used as H_0 in (2), neglecting the small difference between acoustic temperature and virtual temperature, in order to compute ε_o. In the Coorong, where two heights were available, the temperature flux at 2.5 m was used. Then, z_s and u_ε were obtained from (11) and (12), respectively.

In order to convert from frequency n (observed with a fixed sampling rate) to wavenumber κ, the translation speed needs to be defined. While small eddies, in particular those from the inner inertial subrange, quite plausibly travel at the local wind speed $u(z)$, this cannot be expected for the outer eddies. The largest, CBL-spanning, eddies travel at the mean wind speed of the free CBL, u_m. This value is likely to be the upper limit for the translation speed of the heat-transporting eddies. Like ε_o, u_m is not available from measurements within the SFL. On the other hand, based on the notion that z_s sets the minimum size of the attached eddies, it is reasonable to suppose that $u_s = u(z_s)$ is a good approximation of their translation speed. We estimate u_s by extrapolation from the wind speeds measured within the SFL, using the classical surface-layer wind profile for unstable stratification (Paulson 1970). Frequency is then converted to wavenumber by $\kappa = 2\,\pi\, n/u_s$, and κ is non-dimensionalised by multiplication with an appropriate length scale.

Scaling of the spectra, both measured and modelled, was done for each run individually. Scaled spectra were then averaged into classes, as described in Sections 6.1 and 6.2.

5.5 Estimation of CBL depth

In the Coorong experiment, the depth of the CBL was determined twice per day. Aircraft measurements of vertical profiles of temperature and wind speed were collected before and after flying the grid pattern. z_i was then taken as the bottom level of the lowest strongly stable section of the potential temperature profile. For the first four days of measurements, aircraft profiles were either not reaching high enough or showed a complex CBL structure, so that the extent of the outer layer relevant for our scaling purposes was ambiguous. We therefore restrict analysis to the last four days,

when z_i was either approximately constant between profiles (13 October, 725 m) or grew at an average rate, taken linearly in time, that seemed plausible (25 m h^{-1} on 14 October, for an already deep CBL, or 63 m h^{-1} on 15 and 16 October, for the initially shallow CBL shortly after arrival of the sea breeze at the pasture site).

At Aorangi, lack of direct measurements of CBL depth made it necessary to derive this parameter from the frequency of the maximum of the horizontal wind spectrum, n_m, setting $z_i = u/(1.5\ n_m)$. It was found that the 20-min averaging period was in some instances (of low wind speed) too short to do this, and the spectra in general very erratic with multiple peaks, causing frequent ambiguity about n_m. Therefore, u spectra were recalculated for 60-min averaging periods, and instead of simply using the absolute maximum, the first up to six local maxima of the (still erratic) spectrum were considered as candidates for n_m. These candidates were then screened in the context of the likely temporal evolution of the CBL for each day – in other words, the sequence of hourly u spectra of each day was visually examined for persistent features, compatible with knowledge of the heat flux, cloud cover, and wind direction, to select the most likely value for z_i. The hourly means of z_i obtained in this way were assigned to the central 20 min of the hour, and then interpolated between hours to provide intermediate values for the first and last 20-min subperiod of each hour. This procedure, partly subjective, resulted in plausible temporal evolution of CBL depth, with growth in the morning and slow changes (up or down) in the afternoon, as well as in a few instances rather sudden changes associated with wind direction changes (front arrivals). It is possible that occasionally the wrong choice of n_m was made, but because z_i is a fairly conservative variable in the afternoon, and has a fairly predictable growth pattern in the morning, its error is unlikely to be more than 30 %, which should be sufficiently small for the scaling purposes considered below.

6 Results and discussion

Here we describe the CBL conditions for both experiments and, based on this, how the runs were sorted into classes. We then compare key parameters of our new scheme with their Monin-Obukhov counterparts. Next, the temperature spectra are presented and discussed, followed by the heat flux cospectra.

6.1 Aorangi experiment: CBL development and data classification

At Aorangi, the predominant westerly wind directions were usually associated with variable cloud cover, often overcast. The maximum CBL depth, reached in the early afternoon and changing little until evening, was typically 300 to 500 m for these conditions, limited to such rather low values by the influence of the coastline 20 km to the west. On a minority of days, easterly winds prevailed, with less or no cloud cover. Then, z_i reached afternoon values of 600 to 800 m. Within these ranges of variability, the CBL evolution was fairly similar between days. By including runs from the CBL growth phases in the mornings, the total range of z_i values encountered spans about 1.5 decades.

Runs were considered suitable for analysis if they fulfilled the criteria of $u_* > 0.1$ m s^{-1} and $H > 20$ W m^{-2}. Of these runs, many with small z/z_s (potentially very close to neutral stratification) had to be excluded due to significant noise in the temperature spectra. All runs with very small temperature variance ($\sigma_T < 0.15$ K) had noisy T spectra, accounting for half of the excluded runs. Runs with $0.15 < \sigma_T < 0.35$ K were manually screened to exclude those with unacceptable noise levels (accounting for the other half).

A total of 509 runs were accepted. The z/z_s values for these spread from 0.010 to 0.79, with a broad maximum around the average value of 0.13. Only 6 runs were found in the upper half of the SFL ($z/z_s > 0.5$). The data are sorted into five classes, named A to E according to decreasing z/z_s, with the thresholds between classes chosen to compromise between the competing ideals of significantly different z/z_s on the one hand, and similar class sizes (for similar levels of random error) on the other hand. These thresholds are: $z/z_s < 0.04$ for Class E, $0.04 < z/z_s < 0.09$ for D, $0.09 < z/z_s < 0.14$ for C, $0.14 < z/z_s < 0.22$ for B, and $0.22 < z/z_s$ for A. In addition, a Class A* (near SFL centre, $z/z_s > 0.4$) is defined as a sub-class of A rather than a separate class, comprising 14 runs only. This approach spreads the z/z_s range under investigation while keeping the size of Class A large enough to have a level of random error comparable to that of Classes B to E. Table 1 shows class sizes and average values of some SFL parameters. Wind speed and u_* are positively correlated with z_s, while z_i is not – in fact, there a no significant differences in z_i between the classes.

6.2 Coorong experiment: CBL development and data classification

In the Coorong, z/z_s ranged from 0.017 (at $z = 2.5$ m) to 0.52 (at $z = 7.0$ m). The 25 selected runs were sorted into classes A to E as shown in Table 2. The primary classification is comparable to that for Aorangi, but based on z_s rather than z/z_s in order to allow direct assessment of the effect of z. Neighbouring classes differ by about a factor 1.5 to 3, except for Classes B and C, which cover the same range for z_s. These two classes, however, were from days with very different CBL depth, so z_i was used as a secondary sorting parameter. The classification is based on the strong differences in CBL and SFL characteristics between measurement days, as follows.

On 13 October, the outer layer was represented by a well-mixed CBL, with neutral potential temperature profile. This CBL was capped at 725 m by a well-defined strong inversion. Wind speeds within it were high, with $u_s > 11$ m s^{-1}, and consequently, stratification was nearer to neutral than on the other days. Wind direction was steady around 240°. This day provided the runs of Class E.

On 14 October, wind direction was also steady, at 220 (±10)°, but wind speeds were much lower, with $u_s \approx 3$ m s^{-1} until 1300 h, then steadily increasing to about 6 m s^{-1}. When the aircraft arrived at 1050 h, a CBL had already developed up to 1190 m. By 1300 h, this CBL had grown to 1245 m and heated up by about 1 K on average. In the upper half of the CBL the potential temperature profile was slightly stable, with a gradient of 0.6 x 10^{-3} K m^{-1} at 1050 h and 1.4 x 10^{-3} K m^{-1} at 1300 h; in the lower half the profile was neutral. Stratification in the surface layer was moderately to strongly unstable: $-L < 25$ m and, in good accord with (7), $z_s < 28$ m. This day provided the runs of Classes A and B.

By contrast, on 15 and 16 October the CBL was a shallow sea breeze, the sudden arrival of which was detected by the sonic anemometers on both days. On 15 October, this sea breeze arrived at the pasture site at 1332 h. From the aircraft sounding at 1400 h, its depth was obtained as 222 m, indicated both by a sudden increase in potential temperature and a reversal of wind direction. At the end of this day, the aircraft did not fly an ascent high enough to determine CBL depth, which was therefore estimated on the assumption that the CBL growth rate of 16 Oct also applied on 15 October. On 16 October, the depth of the sea breeze layer grew from 80 m at 1200 h to 215 m at 1410 h. The CBL was thus shallower than on 15 October. Values for wind speed and z_s on these two days were intermediate between those of 13 and 14 October. Sorting by z_s, one run from 15 October and three from 16 October form Class C, and four runs from 15 October and one from 16 October form Class D.

804

805 **6.3 Comparison of new and traditional parameters**

806 Section 4.1 concluded noting the "approximate equality" of SFL depth and the
807 (negative) Obukhov length. In Fig. 1 it is shown with what uncertainty this relationship
808 applies to the present two datasets. There, the solid line indicates a slope of 1.1, which
809 would be obtained if $\psi_o = 1.1$, as we assume throughout, and $u_\varepsilon = u_*$. The latter
810 assumption we have avoided, by computing ε from (14) and using (11) to estimate z/z_s.
811 As a result of that procedure, we find $z/z_s \approx -z/L$ only for $-z/L < 0.2$ or so (Fig. 1). By
812 contrast, for $-z/L > 0.2$ we find that $-z/L$ frequently and considerably exceeds z/z_s, and
813 does so with large variability, indicating that the difference between u_ε^3 and u_*^3 is often
814 significant. This implies, firstly, that z/z_s tends to be more constrained at the upper end
815 of its range (here: < 0.8) than $-z/L$ (here: < 3), and secondly, that runs classified as
816 moderately to strongly unstable, according to z/L, spread across all classes of our
817 classification by z/z_s.

818 These results warrant a closer look at u_ε values, which are not included in Tables
819 1 and 2. From (12) it follows that $u_\varepsilon/(k\,\varepsilon\,z)^{1/3} > 1$ for $z/z_s < 0.8$, with a maximum of
820 1.13 at $z/z_s = 0.247$. By implication, in the region $0.1 < z/z_s < 0.3$, where the majority of
821 the Aorangi data are found, u_ε can be expected to exceed u_* typically by 10 %
822 (modifying (7) for that height region to $-z_s/L \approx 1.2$). Fig. 2 shows that the majority of
823 u_ε values, from both experiments, fall indeed between u_* and $1.2\,u_*$, consistent with
824 this expectation and a random error of u_* of order 10 %. However, Fig. 2 also shows
825 that for relatively weak wind speeds ($u_* < 0.3$ m s^{-1}) this orderly relationship between
826 u_* and u_ε disappears and the latter tends to greatly exceed the former, with large
827 variability. It is this variability that explains the enormous scatter in Fig. 1.

828 Also shown in Fig. 1 are dashed lines marking ±70 % deviation from the slope of
829 1.1, indicating the estimated uncertainty of ψ_o and thus ε_o. This uncertainty potentially
830 adds further variability not accounted for in Fig. 1, due to lack of knowledge of true ε_o.

831 To summarise, we find that the relationship (7) is fairly accurate only for
832 moderate to strong, and steady, wind speeds (conditions that cause $-z/L < 0.2$). In
833 general it should be viewed as an order-of-magnitude relationship only. As a
834 consequence, classifications by $-z/L$, commonly found in the literature, can be
835 interpreted as approximations of a z/z_s classification, with the match between the two
836 classifications becoming increasingly poorer as both parameters increase.

837

6.4 Temperature spectra – comparison to the Kansas model

Here we compare our temperature spectra with the "Kansas spectra" of KWIC72, which have become a standard in boundary-layer meteorology. These spectra are normalised according to the rules of the Monin-Obukhov similarity theory (Monin and Obukhov 1954), but with an additional factor $\varphi_N\,\varphi_\varepsilon^{-1/3}$, where φ_ε is given by (3) and φ_N is the dimensionless dissipation of temperature variance. This factor is designed to force collapse of the inertial subranges of the various spectra.

The temperature spectra from Aorangi, scaled with the Kansas scheme, are shown in Fig. 3, and from the Coorong in Figs. 4 and 5, for the classes listed in Tables 1 and 2, respectively. The frequency axis is scaled using measurement height as the length scale and local wind speed at that height as the velocity scale. On the amplitude axis, we include, like KWIC72, the factor $\varphi_N\,\varphi_\varepsilon^{-1/3}$. Assuming local balance between dissipation and 'production', the dimensionless dissipation of temperature variance, φ_N, is substituted by the dimensionless temperature gradient, φ_h, using the best-fit expression of Högström (1988, Eq. 15). SHHS07 followed the same practice. We include in Figs. 3 to 5 a curve describing the range where SHHS07 found the spectra for runs of "unstable, very close to neutral (UVCN)" stratification to collapse. This curve essentially agrees with the Kansas spectrum for $f > 0.7$, but at lower frequencies it has a lower amplitude, with a maximum at $f \approx 0.25$. SHHS07's curve is not extended below $f < 0.15$ because no universal shape was reported there.

The following features are observed in Figs. 3 to 5. First, at low frequencies and in the peak region, the measured spectra fall between the curves marked as "Kansas (neutral)" and "Kansas (max.)". Second, the class with the largest z_s (E) has consistently more power at low frequencies than the other classes, and (if the spectra were smoothed further) would have the lowest peak frequency. By contrast, the class with the smallest z_s (A) displays the highest peak frequency in Figs. 4 and 5, in line with the behaviour observed by KWIC72 and referred to in the first paragraph of Section 1. Third, in the inertial subrange the spectra from the five classes collapse well (except Class E in Fig. 3, due to high-frequency noise) and approach the neutral Kansas model curve, as well as that of SHHS07. Thus, our data are compatible with the data of KWIC72 and, since they do not quite reach into the "UVCN" range, also with those of SHHS07.

KWIC72 fitted the neutral power spectra from Kansas for T and the velocity components to match a slope of 1 for the lower asymptote ($f \to 0$) and a slope of −2/3 for the upper asymptote ($f \to \infty$), and to display a single peak in between. Curiously,

873 the temperature spectrum is the only one for which KWIC72 deviated from the general
874 shape by defining separate branches for lower and higher frequencies, joined at
875 $f = 0.15$ (about twice the peak frequency). The joint of the two branches appears as a
876 slight kink in Figs. 3 to 5, suggesting the possibility of two turbulence regimes (two
877 types of eddies) contributing to the shape of the *T* spectrum. KWIC72 did not discuss
878 this.

879 Figs. 3 to 5 show that, at high frequencies, our *T* spectra converge towards the
880 well-collapsed part of the spectrum observed by SHHS07 (their Figs. 8 and 9) for
881 "UVCN" stratification (indicated with thick dots). In our interpretation, this indicates
882 that inner eddies are – at least approximately – scaled correctly with the traditional
883 (inner) scaling parameters. However, at low frequencies and in the peak region, where
884 we expect outer eddies to be the main agents of transport, inner scaling is unable to
885 provide a universal description of the *T* spectrum.

886

887 **6.5 Temperature spectra – scaling with the impinging-eddies model**

888 When scaling spectra (or cospectra) with the impinging-eddies model, as in this and
889 the following subsection, we are interested in collapsing the peak positions between
890 different classes and different experiments. Model spectra have a single and
891 unambiguous peak, which separates a low-wavenumber flank, where the general trend
892 of the amplitude is to increase, and a high-wavenumber flank, where the general trend
893 is to decrease. By contrast, observed spectra display some degree of raggedness
894 throughout (particular those from the Coorong, due to the small number of runs in each
895 class). This raggedness does not mask the general trends on the flanks, but it leads to
896 some ambiguity about the peak coordinates: the spectra have a "peak region" with
897 multiple local maxima, usually not far apart. One could apply a smoothing procedure
898 to reduce such ragged regions to single peaks, but we decided against that because
899 such manipulation would remove the reader a step further from seeing the original
900 results. Instead, we will use the term "peak" somewhat loosely to describe a smoothed
901 hypothetical maximum, in the centre of the "peak region". This "peak" can also be
902 viewed as the location where the extrapolated trends of the two flanks would intersect.
903 In effect, the reader is expected to do some smoothing of the peak region by eye. We
904 claim good collapse of observed spectra on the wavenumber axis when large fractions
905 of their peak regions overlap, and we claim a match with a model curve when the peak
906 position of the latter sits well within that peak region. On the amplitude axis, we claim

907 good collapse on a smoothed-by-eye basis. Even without defining a smoothing
908 procedure, this is in practice well enough constrained, given the considerable
909 uncertainties of the scaling parameters. These uncertainties are discussed further
910 below.

911 Our hypothesis is that attached outer eddies of scale z_s transport heat through
912 most of the depth of the SFL. What is not yet clear is how to implement this
913 hypothesis. Rather than present our solution to this problem directly, we first show a
914 result from an earlier stage of our empirical investigation. In Fig. 6, the temperature
915 spectra are scaled with the parameters that MCM07 found to collapse the peak regions
916 of T spectra above the SFL, i.e. a velocity scale $(z\,\varepsilon_o)^{2/3}$ on the amplitude axis and a
917 mixed length scale $(z_i\,z)^{1/2}$ on the wavenumber axis. This scaling produces a family of
918 spectra whose peak positions, on both axes, systematically approach the peak of
919 MCM07's spectrum as z/z_s increases. This is encouraging orderliness, by contrast to
920 Figs. 3 to 5, but it is clear that we must introduce a dependence on z/z_s into the scales
921 for both axes if we are to turn orderly progression into collapse.

922 Since our model expects z_s to be the length scale of the transporting eddies rather
923 than z, we replace z with z_s on the wavenumber axis, giving a mixed length scale
924 $(z_i\,z_s)^{1/2}$. The visual impression of this scaling for the Aorangi data (Fig. 7) is excellent
925 collapse of peak positions between classes, as well as excellent match with the above-
926 SFL value of 4.83. For the Coorong (Figs. 8 and 9), the spread between classes appears
927 wider, but the overall match with the above-SFL value is still good. For the amplitude
928 axis we proceed empirically, finding good collapse with each other, as well as best
929 match with the above-SFL value of 0.7, when using $(z_s\,z)^{1/3}\,\varepsilon_o{}^{2/3}$, as shown in Figs. 7 to
930 9. To quantify the visual impressions, we discuss the uncertainty of the scaling on both
931 axes next.

932 The largest parameter error can be attributed to ε_o, of order ±70 %. Since
933 $z_s \propto \varepsilon_o{}^{-1}$, in first-order approximation of (10), the amplitude scaling with $z_s{}^{1/3}\,\varepsilon_o{}^{2/3}$ is
934 uncertain by about 25 %. The scaled amplitudes for Aorangi do indeed agree with
935 MCM07 within 15 %, and for Coorong within 25 %. Also, the error of ε_o may conceal
936 systematic trends, because the real ε_o depends on variables that were not measured,
937 like entrainment of kinetic energy. This might explain why the classes with $z/z_s > 0.4$
938 (A* for Aorangi, Fig. 7; A for Coorong at 7.0 m, Fig. 8) have lower amplitudes than
939 the others.

On the wavenumber axis, ±30 % error of $z_s^{1/2}$ is due to the uncertainty of ε_o. This error component alone can thus explain the observed spread of ca. 20 % between peaks at Aorangi (Fig. 7). For the Coorong, adding rough error estimates of 10 % for $z_i^{1/2}$ and 20 % for u_s (since $\kappa \propto u_s^{-1}$) results in a total mean square-root error of order 40 %, which is similar to the observed spread of the "peaks" (in the sense explained at the start of this section) in Figs. 8 and 9. In addition, potential inaccuracy of the assumed ε profile (10), particularly in the region $0.1 < z/z_s < 0.3$, may have caused bias of z_s.

Overall, it is concluded that the scaling in Figs. 7 to 9 achieves peak collapse on both axes within experimental error. A cautious estimate of the scaled peak wavenumber is $\kappa\,(z_i\,z_s)^{1/2} = 4.5\ (\pm 1.5)$, which agrees with the peak location that MCM07 found above the SFL on a $\kappa\,(z_i\,z)^{1/2}$ axis (their Fig. 8). Our best estimate for the peak amplitude, scaled with $(z_s\,z)^{1/3}\,\varepsilon_o^{2/3}/\overline{w'T'}^{\,2}$, is 0.7 (±0.1), also in agreement with the above-SFL results if z_s is replaced by z. The proposed scaling thus produces results that are consistent between the two present datasets and, via a smooth parameter transition for $z \to z_s$, with MCM07. This consistency means considerable improvement over the Kansas model, which does not predict exact peak locations or amplitudes but only a region (shaped as a curved band in frequency-amplitude space) into which the spectra are expected to fall.

The mixed length scale on the wavenumber axis, in our interpretation, describes z_s-scale eddies (the smallest outer eddies that survive interaction with inner eddies) that are organised into a pattern by the largest eddies that can exist in the CBL, of z_i-scale. Though there is no mathematical theorem that says so, the pattern found in the present data and by MCM07 seems to be that a mixed length scale is always the geometric mean of the interacting scales. "Interaction" may mean that the larger-scale process modulates or organises the processes at the smaller scale.

On the amplitude axis, the mixed energy (velocity) scale $(z_s\,z)^{1/3}\,\varepsilon_o^{2/3}$ can be interpreted as follows. Our hypothesis from Section 3.5 is that heat transport in the SFL is predominantly by z_s-scale eddies, which would suggest a velocity scale $(z_s\,\varepsilon_o)^{2/3}$. However, the vertical motion of these eddies is blocked by the ground, and the strength of the blocking effect must be a function of z/z_s. The empirically found velocity scale from Figs. 7 to 9 can be rewritten as $(z_s\,\varepsilon_o)^{2/3}\,(z/z_s)^{1/3}$, suggesting that blocking introduces the factor $(z/z_s)^{1/3}$ to the amplitude scaling, so that the plume velocity approaches zero at the ground. An analogy for this behaviour was observed by MCM07 above the SFL. They found that for small wavenumbers, on a $(\kappa\,z_i)$-abscissa, an amplitude scaling factor of $(z_i\,\varepsilon_o)^{2/3}\,(z/z_i)^{1/3}$ collapses the temperature spectra (their

Fig. 9). They interpret this to describe CBL-spanning eddies with a velocity scale $(z_i\,\varepsilon_o)^{2/3}$ that are blocked by the ground, with a blocking factor $(z/z_i)^{1/3}$. The form of the amplitude scaling factor is consistent between MCM07 and the present data, except that in their case it applies to z_i-scale eddies and in the present data to z_s-scale eddies. The appearance of z in the amplitude scaling factor, therefore, does not represent the action of inner eddies but describes the blocking of the outer eddies by the ground.

Apart from the successful collapse of peak locations, Fig. 7 has another distinct feature: as z/z_s decreases successively from Class A* to E, the amplitude of the high-wavenumber flank, for $\kappa\, z_i^{1/2}\, z_s^{1/2} > 30$, systematically increases. In Figs. 8 and 9, the systematic increase in amplitude at high wavenumbers is less certain than in Fig. 7, probably because it is masked by errors in wavenumber scaling. The systematic progression with z/z_s for large wavenumbers in Fig. 7 can be converted to a collapse of curves by changing the length scale on the wavenumber axis to $z_i^{1/4}\, z_s^{1/4}\, z^{1/2}$ (Fig. 10). This new length scale can be rewritten as $[(z_i\, z_s)^{1/2}\, z]^{1/2}$, suggesting that it mixes a simple length scale (z) with one that is itself mixed already. It collapses Classes B to E well for $7 < \kappa\, z_i^{1/4}\, z_s^{1/4}\, z^{1/2} < 70$, and the reason for lack of collapse at even larger wavenumbers is, very likely, instrumental noise. The obvious outlier is Class A. This class shows, in Fig. 7 already, a lower amplitude than the other classes throughout all wavenumbers, which, as argued above, may be due to systematic error of ε_o. If this explanation is correct, then the Class A spectrum should be rescaled so that its peak height approximately matches the peak heights of Classes B to D in Fig. 7. Such a rescaling would remove the mismatch at large scaled wavenumbers in Fig. 10, too, resulting in collapse of all classes within experimental error.

The doubly-mixed wavenumber scaling in Fig. 10 provides a smooth transition of scaling parameters at the top of the SFL. As before with the peak scaling, if z_s is replaced by z on both axes for $z/z_s > 1$, then the results of MCM07 are reproduced. In their Fig. 10, all spectra collapse onto a line described by the function $b\,(\kappa\, z_i^{1/4}\, z^{3/4})^{-2/3}$, where $b = 2.63\ (\pm 0.07)$, for the range $\kappa\, z_i^{1/4}\, z^{3/4} > 20$. Our Fig. 10 shows the corresponding function for the doubly-mixed length scale, with the same amplitude factor b, and we find that this function matches the spectra of Classes B to E well, for scaled wavenumbers > 20. This quantitative consistency with MCM07 is further support for the suggested doubly-mixed length scale.

To interpret this doubly-mixed scale, we note that, in this wavenumber range, the eddies acting on the temperature field are detached eddies of the inner Richardson cascade, with sizes scaling on z. We expect these eddies to shred the margins of the

larger plumes. In other words, we expect an interaction between the plumes scaling on the mixed length scale $(z_i\, z_s)^{1/2}$ and the eroding eddies of z-scale. Again, we find that interactions produce mixed length scales which are the geometric mean of the interacting length scales. This explanation is the same as that offered by MCM07 for their mixed scale $z_i^{1/4}\, z^{3/4}$ in the corresponding wavenumber range region above the SFL (their Fig. 10). We further note that in both cases the velocity scale on the amplitude axis needed to collapse the large-wavenumber regions is the same that successfully collapses the peak regions, indicating that the shredded filaments travel with the rising main plumes.

6.6 Scaling of heat flux cospectra

For the heat flux cospectra there seems to be no alternative to scaling the ordinate on the total heat flux at the ground, though this scales the area under the spectrum (in semi-logarithmic presentation) rather than the peak amplitude. For this reason, if there is a difference in amplitude between two cospectra in one waveband, there must be a balancing difference in cospectral amplitude at other wavebands. Therefore we do not expect perfect collapse of peak heights and concentrate on peak wavenumbers.

Again there is a question about how to implement our conceptual model, and again we test a number of alternative scaling schemes. We begin by using the mixed length scale that successfully collapses the positions of the peaks of the T spectra, $z_i^{1/2}\, z_s^{1/2}$. This tests the proposition that the lengths and aggregations of the flux-carrying structures are the same as those of the temperature structures themselves. We find that collapse in peak positions between the classes is not as good as for the T spectra. There is a clear trend for smaller z/z_s being associated with higher peak wavenumbers in the Aorangi data (not shown) – in fact not only the peak region, but the whole spectrum shifts systematically upwards as z/z_s decreases. In the Coorong, a similar systematic shift with z/z_s is not observed (Fig. 11). The cospectra agree with those from Aorangi in that Class E has the flattest and widest shape and the largest peak wavenumber, and that for Classes D and C (increasing z/z_s) the peak wavenumber decreases to approach that found for the T spectra. However, as z/z_s increases further (B and A), the peak wavenumber increases again. In the Coorong, a major difference between Classes D and C on the one hand and B and A on the other is that the former represent small and the latter large z_i, so it seems that the influence of z_i on the wavenumber scaling has been exaggerated with an exponent of 1/2. Further, the peak

wavenumbers for $z = 7.0$ m (not shown) are consistently smaller than those for $z = 2.5$ m (Fig. 11), suggesting that z should be included in the length scale.

These observations lead us to test the doubly-mixed length scale that collapses the large-wavenumber ranges of the T spectra, $z_i^{1/4}\, z_s^{1/4}\, z^{1/2}$. Both for Aorangi (Fig. 12) and for the Coorong (Figs. 13 and 14) this length scale successfully collapses the peaks of the cospectra of Classes A to D. Of particular note is that the peaks are in the same position in all three plots, at a scaled wavenumber of about 1.2 (±0.3).

The appearance of the doubly-mixed length scale is interpreted as follows. The heat-transporting entities are not simply the whole $(z_i^{1/2}\, z_s^{1/2})$-scale plumes as detected by their temperature signatures, but z-scale structures acting within the context of the $(z_i^{1/2}\, z_s^{1/2})$-scale plumes. This involvement of z-scale eddies helps to explain how heat transport in $(z_i^{1/2}\, z_s^{1/2})$-scale plumes can be so effective at heights down to only a few percent of z_s. It appears that there are z-scale eddies within z_s-scale eddies within z_i-scale eddies, and these sweep up plumes within plumes within plumes, with a handover of heat upwards from one scale to another, and a handover of organisation downwards from one scale to another. This can be described as a top-down organisation of a bottom-up heat flux, extending right down almost to the smallest scales.

At very small z/z_s the doubly-mixed scale fails to collapse the cospectral peaks. The Class E cospectrum from Aorangi (Fig. 12), for which mean $z/z_s = 0.027$, shows a plateau instead of a clear peak that spans the range $1 < \kappa\, (z_i^{1/4}\, z_s^{1/4}\, z^{1/2}) < 12$, and in the Class E cospectrum from the Coorong at 2.5 m (Fig. 14), for which mean $z/z_s = 0.023$, a distinct peak emerges at the upper end of this range, on top of a similar plateau. The small values of z/z_s place these observations within the near-ground layer where simple inner scaling is expected (Kader and Yaglom 1990). Inner scaling implies that the acting eddies are of z-scale. To test this scaling, the cospectra from the Coorong at 2.5 m are shown on a $(\kappa\, z)$ abscissa in Fig. 15, together with the neutral (0^+) Kansas cospectrum. $\kappa\, z$ differs from the normalised frequency f in "Kansas scaling" (KWIC72) only by the factor $2\, \pi\, u/u_s$. For Class E, $u/u_s = 0.67$, while for Class A, $u/u_s = 0.82$. This spread is visualised by the thickness of the Kansas model curve in Fig. 15. The peak of Class E is located at $\kappa\, z = 1.1$ (±0.2), so in Kansas scaling, the peak location would be at $f \approx 0.26$. This agrees excellently with the position where SHHS07 find peaks in their cospectra for "unstable, very close to neutral" stratification. It also matches the cospectral peak position of "BOMEX data" that "show considerable departure" (from the 0^+ curve), reported by KWIC72 in their Fig. 14.

Not only does the (κz)-scaling in Fig. 15 lead to agreement of the peak location of Class E with the peak locations in BOMEX and SHHS07, but at this peak location we also observe an orderly trend of the cospectral amplitude to decrease with increasing z/z_s (from Class E to A). This trend is opposite to that in the region where Classes A to D have their peaks (at $\kappa z \approx 0.2$, but as shown in Figs. 12 to 14, properly scaled with the doubly-mixed length scale). Our interpretation of this pattern is that the heat flux cospectrum is generally composed of two contributions: one from the plumes organised by outer eddies, as described above, and one from the inner eddies. It is likely that the two contributions reflect not coexistence of different eddy processes in the same place and time, which is unlikely in such a non-linear system, but alternation in time as the energy of the inner eddies track outer-scale variations in wind speed and shear stress. The two contributions are of equal strength for $z/z_s \approx 0.03$, and the trend suggests that the inner scaling will dominate at lower z/z_s. Inner scaling occurs at wavenumbers associated with the action of detached eddies. These are the largest wavenumbers in every cospectrum, as evident from the asymptotic collapse of all classes at large κz (Fig. 15). At these wavenumbers, the contribution to the heat flux depends only on the sizes and energies of the local detached eddies, which implies that this contribution may be modelled using a mixing-length model. However, this is not true for the larger-scale contributions to heat transport, which are organised in top-down fashion.

The pattern in Fig. 15 of two preferred peak locations, with a systematic transition between them, is similar to that reported by SHHS07. Such a pattern may also have been present at Kansas, but was probably missed by KWIC72 because they did not use a z/z_s classification. They did report the range of variability, though: the unstable heat flux cospectra at Kansas fell into a band either side of the neutral (0^+) curve, with possible peak amplitudes within that band ranging from ca. 0.15 to 0.3, at peak locations $0.02 < f < 0.3$. These ranges are fully compatible with the present observations. Fig. 15 suggests that the neutral Kansas curve does not represent the true shape of any single cospectrum, but is a compromise between, or a composite of, many runs with peaks that did not collapse with each other. At a time when surface-layer turbulence was considered to have a single dominant length scale, and spectra and cospectra were accordingly fitted with single-peaked functions, this was probably an inevitable outcome.

7 Conclusions

In this paper we have continued the development of the turbulence model of McNaughton (2004a, b, 2006) and MCM07 by applying it to heat transport within the SFL, of depth z_s. We have presented temperature spectra and heat flux cospectra from observations made within the SFL, at two different sites. Using the same methods for scaling analysis as used by MCM07, we find that:

- The positions of the peaks of temperature spectra collapse, for the whole range of z/z_s encountered ($0.01 < z/z_s < 0.79$), when wavenumbers are scaled with the geometric mean of z_s and CBL depth, z_i. The scaled peak wavenumber is $\kappa\,(z_i\,z_s)^{1/2} = 4.5\ (\pm 1.5)$.
- The heights of the peaks of temperature spectra collapse when wavenumbers are scaled using $(z_s^{1/2}\,z^{1/2})^{2/3}\,\varepsilon_o^{2/3}/\overline{w'T'}^{\,2}$, at a value of 0.7 (±0.1).
- There is evidence that at the larger wavenumbers associated with the action of detached eddies, the temperature spectra collapse when amplitudes are scaled in the same way as for the peak region, and wavenumbers are scaled using the doubly-mixed length scale $z_i^{1/4}\,z_s^{1/4}\,z^{1/2}$.
- As z approaches z_s, the new scaling scheme provides a smooth transition to the above-SFL scaling of spectral peaks found by MCM07, with z_s being replaced by z in the scaling factors on both axes.
- The positions of the peaks of the heat flux cospectra collapse, for $z/z_s > 0.03$, when wavenumbers are scaled using the doubly-mixed length scale $z_i^{1/4}\,z_s^{1/4}\,z^{1/2}$, at a scaled peak wavenumber of 1.2 (±0.3).
- At the larger wavenumbers associated with the action of detached eddies, the heat flux cospectra collapse when wavenumbers are scaled with the inner scale z. For $z/z_s < 0.03$, this wavenumber range contains the cospectral peak, at $\kappa\,z = 1.1\ (\pm 0.2)$.
- As z/z_s decreases, the cospectral amplitude at the location of the "mixed" cospectral peak decreases, while the amplitude at the location of the "inner" peak increases. For $z/z_s \approx 0.03$, the amplitudes at both locations are about equal.

The above observations are fully compatible with the results of SHHS07, and compatible with the results of KWIC72 when the limitations of their analysis are taken into account.

Kader and Yaglom (1990) divided the lower CBL into a dynamic sublayer, a convective-dynamic sublayer and a convective sublayer. This division is compatible with our observations: the dynamic sublayer can be identified as the layer up to $z/z_s \approx 0.03$, where inner scaling dominates all statistics, the convective-dynamic sublayer is the layer $0.03 < z/z_s < 1$, where momentum transport is dominated by inner eddies while heat transport is under the mixed control of inner and outer eddies, and the dynamic sublayer is the layer above the SFL, where all transport is by outer eddies.

In terms of model development, the present results are fully consistent with the earlier results and predictions in the model of the eddy and plume processes developed by McNaughton (2004a,b, 2006) and MCM07. In particular, they are fully consistent with the prediction that the smallest outer eddies that can penetrate the SFL without strong interaction with the inner eddies have lengths that scale on z_s. Not only does z_s set the lengths of the thermal structures (plumes) observed within the SFL, but it also plays a role in setting the vertical velocities of those plumes. Taking note of the present results, we propose an important refinement of the model: it is not the impinging outer eddies that directly transport heat through most of the SFL, but *z*-scale inner eddies acting within the plume structures which themselves are organised, in top-down fashion, by the impinging outer eddies. This modification is significant in that it provides an intermediate mechanism for the hand-over in scale of heat, from the *z*-scale plumes of size $\approx 0.03\, z_s$ in the dynamic sublayer to the $(z_i^{1/2}\, z_s^{1/2})$-scale plumes observed at the top of the SFL.

Further experiments to test our new scaling scheme are highly desirable. Such experiments should be designed to address two shortcomings of the present data. First, the parameters of the outer layer, ε_o and z_i, should be measured directly. Of these two, ε_o is the crucial one, both because it influences the values of the SFL parameters z_s and u_ε, and because little is known about the "climatology" of ε_o in general and the range of validity of the indirect parameterisation discussed in Section 4.1. By comparison, z_i can be fairly well inferred from indirect methods, and plays only a limited role in the wavenumber scaling (though it will also affect the amplitude scaling of horizontal wind spectra, not discussed here). Second, the suggested shape of the dissipation profile within the SFL, $\varepsilon/\varepsilon_o(z/z_s)$, should be tested and refined by measurements, in order to improve the accuracy of the z_s estimation.

In principle, there is no feature in the new scaling scheme that would prevent it from being applied to scalar variables other than temperature. However, in practice one needs to carefully consider to what extent a change in scalar "concentration" across the

CBL top, and resulting entrainment flux of that scalar, acts as an additional source of (co-)variance that affects the (co-)spectral scaling.

Acknowledgements Most of this work was funded by the Marsden Fund of the Royal Society of New Zealand, except for the Aorangi experiment, which was funded by the Foundation of Research, Science and Technology. We thank Jörg Hacker of Airborne Research Australia–Flinders University for operating the aircraft and processing the aircraft data. Tony McSeveny (Landcare Research) helped setting up in both experiments. Hort Research (Kerikeri, New Zealand) and Prof. John Wilson (University of Alberta, Edmonton, Canada) each lent us a CSAT-3 sonic anemometer. We are grateful to the Birks family to allow the Coorong experiment to be conducted on their land, and to the Aorangi Farm staff for logistical support.

References

Antonia RA, Chambers AJ, Friehe CA, van Atta CW (1979) Temperature ramps in the atmospheric surface layer. J Atmos Sci 36:99-108

Bodenschatz E, Pesch W, Ahlers G (2000) Recent developments in Rayleigh-Bénard convection. Annu Rev Fluid Mech 32:709-778

Edson JB, Fairall CW (1998) Similarity relationships in the marine atmospheric surface layer for terms in the TKE and scalar variance budgets. J Atmos Sci 55:2311-2327

Farge M, Pellegrino G, Schneider K (2001) Coherent vortex extraction in 3D turbulent flows using orthonormal wavelets. Phys Rev Lett 87:0545011-4

Ferrare RA, Schols JL, Eloranta, EW, Coulter R (1991) Lidar observations of banded convection during BLX83. J Appl Meteorol 30:312-326

Foster RC (2005) Why rolls are prevalent in the hurricane boundary layer. J Atmos Sci 62:2647-2661

Grinsted A, Moore JC, Jevrejeva S (2004) Application of the cross wavelet transform and wavelet coherence to geophysical time series. Nonlin Processes Geophys 11:561-566

Hacker JM, Crawford TL (1999) The BAT-probe: The ultimate tool to measure turbulence from any kind of aircraft (or sailplane). J Tech Soaring XXIII(2): 43-46

Högström U (1988) Non-dimensional wind and temperature profiles in the atmospheric surface layer: A re-evaluation. Boundary-Layer Meteorol 42:55-78

Hommema SE, Adrian RJ (2003) Packet structure of surface eddies in the atmospheric boundary layer. Boundary-Layer Meteorol 106:147-170

Horst TW, Oncley SP (2006) Corrections to inertial-range power spectra measured by CSAT3 and Solent sonic anemometers, 1. Path-averaging errors. Boundary-Layer Meteorol 119:375–395

Jiménez J (1999) The physics of wall turbulence. Physica A 263:252-262

1222 Kader BA, Yaglom AM (1990) Mean fields and fluctuation moments in unstably stratified
1223 turbulent boundary layers. J Fluid Mech 212:637-662
1224 Kaimal JC, Wyngaard JC, Izumi Y, Coté OR (1972) Spectral characteristics of surface-layer
1225 turbulence. Quart J Roy Meteorol Soc 98:563-589
1226 Kaimal JC, Wyngaard JC, Haugen DA, Coté OR, Izumi Y, Caughey SJ, Readings CJ (1976)
1227 Turbulence structure in the convective boundary layer. J Atmos Sci 33:2152-2169.
1228 Katul G, Kuhn G, Schieldge J, Hsieh C-I (1997) The ejection-sweep character of scalar fluxes
1229 in the unstable surface layer. Boundary-Layer Meteorol 83:1-26
1230 Kays WM (1994) Turbulent Prandtl Number – Where are we? ASME J Heat Transfer
1231 116:284-295
1232 Lin C (2000) Local pressure transport structure in a convective atmospheric boundary layer.
1233 Phys Fluids 12:1112-1128
1234 Lucarini V (2009) Thermodynamic efficiency and entropy production in the climate system.
1235 Eprint arXiv:0901.1993v2, 13pp.
1236 Lumley JL, Panofsky HA (1964) The structure of atmospheric turbulence. Wiley –
1237 Interscience, New York, 239 pp.
1238 Mahrt L, Howell JF (1994) The influence of coherent structures and microfronts on scaling
1239 laws using global and local transforms. J Fluid Mech 260:247-270
1240 Mason RA, Shirer HN, Wells R, Young GS (2002) Vertical transports by plumes within the
1241 moderately convective marine atmospheric surface layer. J Atmos Sci 59:1337-1355
1242 McNaughton KG (2004a) Attached eddies and production spectra in the atmospheric
1243 logarithmic layer. Boundary-Layer Meteorol 111:1-18
1244 McNaughton KG (2004b) Turbulence structure of the unstable atmospheric surface layer and
1245 transition to the outer layer. Boundary-Layer Meteorol 112:199-221
1246 McNaughton KG (2006) On the kinetic energy budget of the unstable atmospheric surface
1247 layer. Boundary-Layer Meteorol 118:83-107
1248 McNaughton KG, Clement RJ, Moncrieff JB (2007) Scaling properties of velocity and
1249 temperature spectra above the surface friction layer in a convective atmospheric
1250 boundary layer. Nonlin Processes Geophys 14:257-271
1251 Melfi SH, Spinhirne JD, Chou S-H, Palm SP (1985) Lidar observations of vertically organized
1252 convection in the planetary boundary layer over the ocean. J Clim Appl Meteorol
1253 24:806-821
1254 Monin AS, Obukhov AM (1954) Basic laws of turbulent mixing in the near-surface layer of
1255 the atmosphere (in Russian). Trudy Geofiz Inst Akad Nauk SSSR 24(151):163-187
1256 Obukhov AM (1946) Turbulence in an atmosphere with a non-uniform temperature (in
1257 Russian). Trudy Inst Teor Geofiz Akad Nauk SSSR 1:95-115. English translation in:
1258 Obukhov AM (1971), Boundary-Layer Meteorol 2:7-29
1259 Ozawa H, Ohmura A, Lorenz RD, Pujol T (2003) The second law of thermodynamics and the
1260 global climate system: a review of the maximum entropy production principle. Rev
1261 Geophysics 41:1018, 24pp.
1262 Paulson CA (1970) The mathematical representation of wind speed and temperature in the
1263 unstable atmospheric surface layer. J Appl. Meteorol. 9:857-861
1264 Perry AE, Chong MS (1982) On the mechanism of wall turbulence. J Fluid Mech 119:173-217
1265 Puthenveettil BA, Arakeri JH (2005) Plume structure in high-Rayleigh-number convection. J
1266 Fluid Mech 542:217-249
1267 Richardson LF (1920) The supply of energy from and to atmospheric eddies. Proc R Soc Lond
1268 A 97:354-373

Schols JLJ, Jansen AE, Krom JG (1985) Characteristics of turbulent structures in the unstable atmospheric surface layer. Boundary-Layer Meteorol 33:173-196

Smedman A-S, Högström U, Hunt JCR, Sahlée E (2007) Heat/mass transfer in the slightly unstable atmospheric surface layer. Quart J Roy Meteorol Soc 133:37-51

Sreenivasan KR (1995) On the universality of the Kolmogorov constant. Phys Fluids 7:2778-2784

Tennekes H (1970) Free convection in the turbulent Ekman layer of the atmosphere. J Atmos Sci 27:1027-1034

Thiermann V, Grassl H (1992) The measurement of turbulent surface-layer fluxes by use of bichromatic scintillation. Boundary-Layer Meteorol 58:367-389

Townsend AA (1951) The structure of the turbulent boundary layer. Proc Cambridge Phil Soc 47:375-395

Townsend AA (1976) The Structure of Turbulent Shear Flow. Cambridge University Press, Cambridge, 429pp.

Wyngaard JC, Coté OR (1971) The budgets of turbulent kinetic energy and temperature variance in the atmospheric surface layer. J Atmos Sci 28:190-201

Zhuang Y (1995) Dynamics and energetics of convective plumes in the atmospheric surface layer. J Atmos Sci 52:1712-1722

Tables

Table 1 Classification of 20-min runs for Aorangi, according to the SFL depth, z_s. Class A* is a sub-class of A, representing measurements near the SFL centre. z_i is CBL depth. u_s is the mean translation speed of eddy structures, assumed as $u(z_s)$. For each class, means and standard deviations (in parentheses) of the parameter values are shown. Measurement height was 3.85 m.

Class	No. Runs	z_s (m)	z_i (m)	z_i / z_s	u_s (m s^{-1})	u_* (m s^{-1})
A*	14	7.9 (1.3)	318 (173)	41 (21)	2.0 (0.8)	0.20 (0.06)
A	66	13.4 (3.5)	349 (163)	28 (15)	2.9 (1.2)	0.22 (0.07)
B	109	22.0 (2.9)	347 (152)	16.1 (7.5)	3.7 (1.5)	0.24 (0.08)
C	108	34.9 (4.8)	366 (159)	10.6 (4.7)	5.3 (2.1)	0.31 (0.10)
D	139	63 (16)	386 (151)	6.6 (3.3)	6.8 (2.4)	0.37 (0.10)
E	87	158 (56)	315 (109)	2.2 (1.1)	11.0 (4.1)	0.53 (0.17)

Table 2 Classification of 30-min runs for Coorong, primarily according to SFL depth, z_s, and secondarily, between Classes B and C, according to CBL depth, z_i. u_s is the mean translation speed of eddy structures, assumed as $u(z_s)$. For each class, means and standard deviations (in parentheses) of the parameter values are shown, except for z_i in Class E, which is assumed constant. Measurement heights were 2.5 and 7.0 m.

Class	No. Runs	z_s (m)	z_i (m)	z_i / z_s	u_s (m s^{-1})	u_* (m s^{-1})	Comments
A	6	14.6 (2.4)	1226 (30)	86 (15)	3.4 (0.4)	0.26 (0.03)	deep CBL
B	4	22.8 (3.9)	1273 (33)	57 (9)	5.0 (1.1)	0.34 (0.05)	deep CBL
C	4	23.3 (5.1)	200 (35)	8.9 (2.3)	5.6 (0.7)	0.36 (0.03)	developing sea breeze
D	5	38.4 (8.2)	277 (91)	7.1 (2.0)	6.4 (0.2)	0.39 (0.02)	developing sea breeze
E	6	112 (17)	725	6.6 (0.9)	11.7 (0.5)	0.56 (0.03)	steady sea breeze

Figures

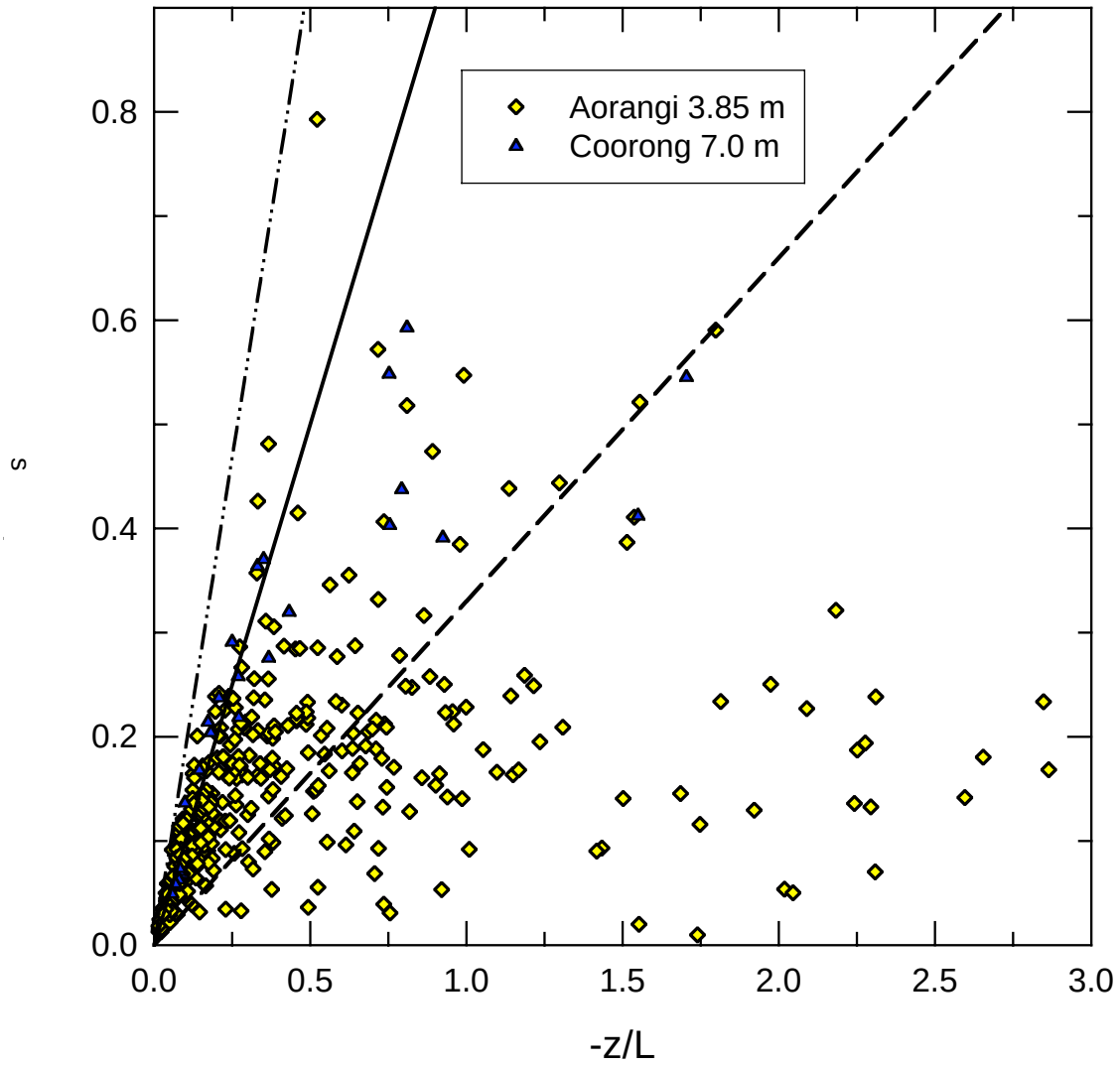

Fig. 1 Scaling parameter z/z_s compared to Monin-Obukhov scaling parameter $-z/L$, for Aorangi (diamonds) and Coorong (triangles). The solid line represents $z/z_s = -1.1\ z/L$, with ±70 % error limits indicated by dashed lines.

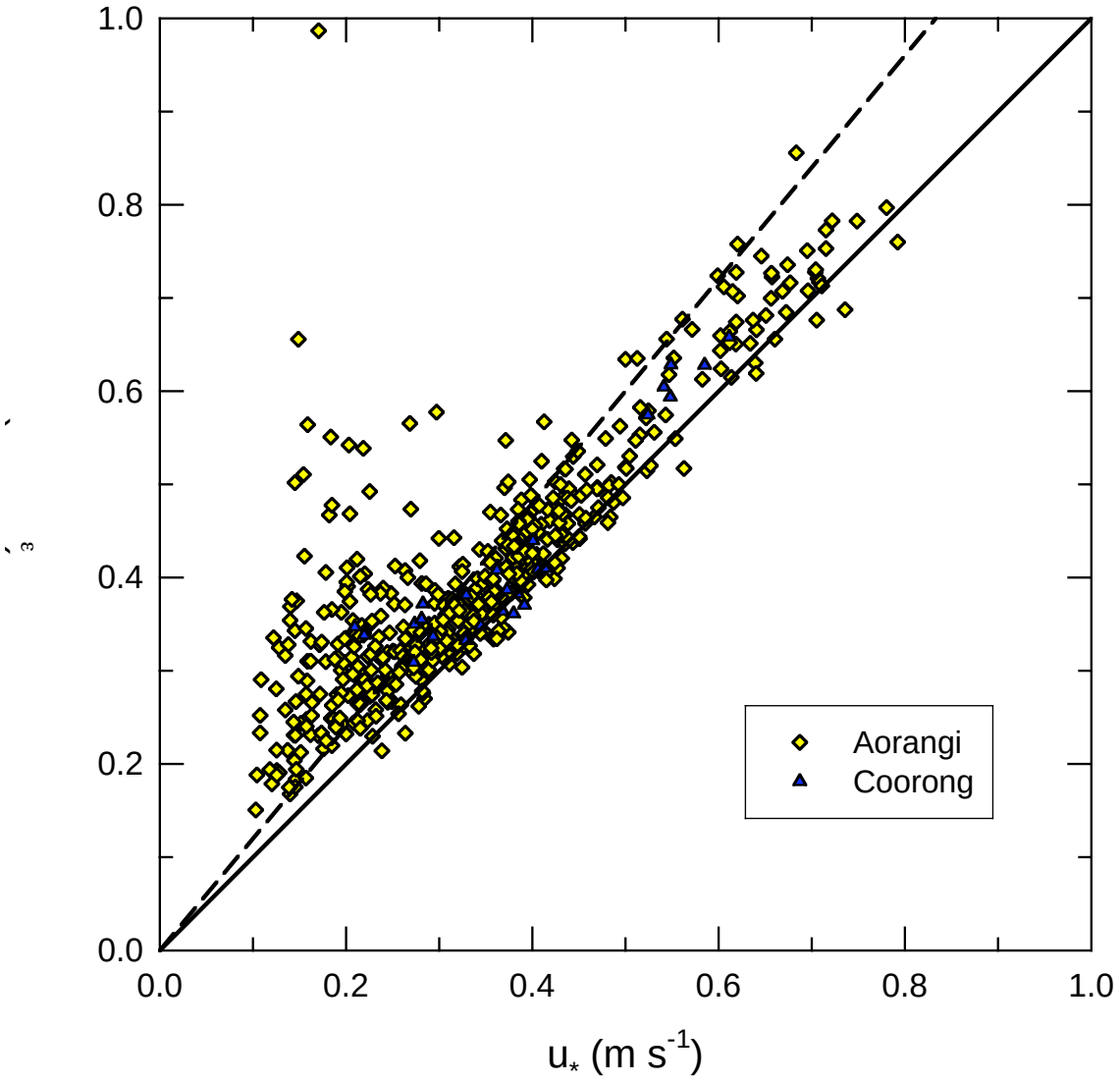

Fig. 2 Dissipation velocity compared to friction velocity, for Aorangi (diamonds) and Coorong (triangles). The solid line represents $u_\varepsilon = u_*$ and the dashed line $u_\varepsilon = 1.2\ u_*$.

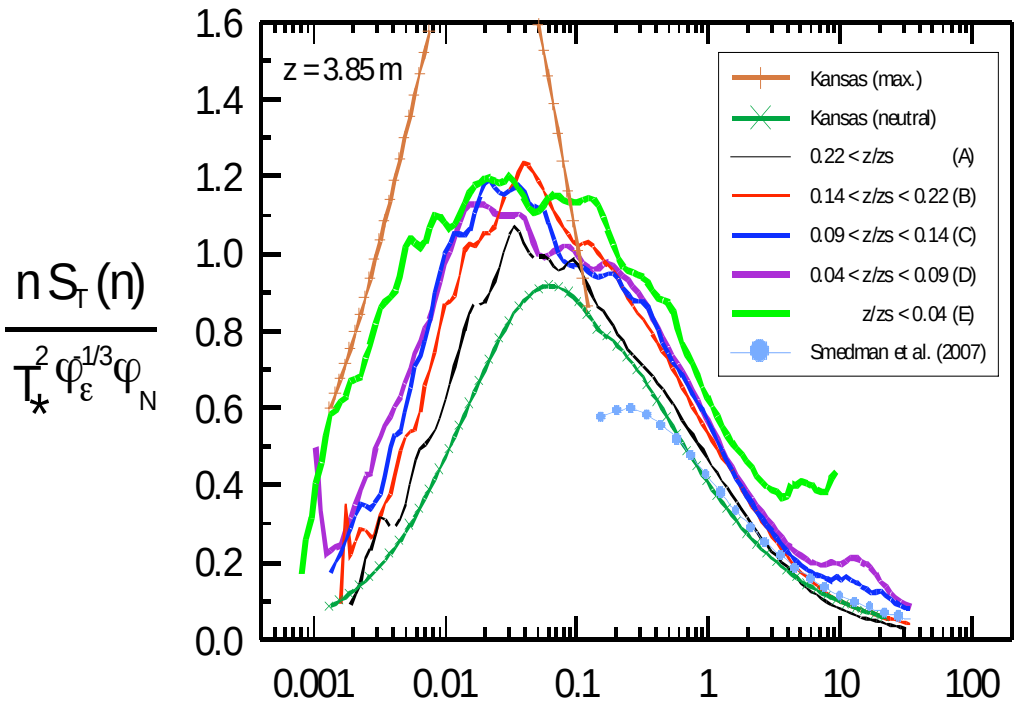

Fig. 3 Temperature spectra for Aorangi, scaled with stability-dependent factors on the amplitude axis and local wind speed on the frequency axis. The spectra are averaged separately for five classes (A to E) defined in Table 1. Also shown are the neutral (0^+) Kansas spectrum, the upper limit of the unstable range found at Kansas (Kaimal et al. 1972), and the "unstable very close to neutral" spectrum of Smedman et al. (2007) for $n\,z/u > 0.15$.

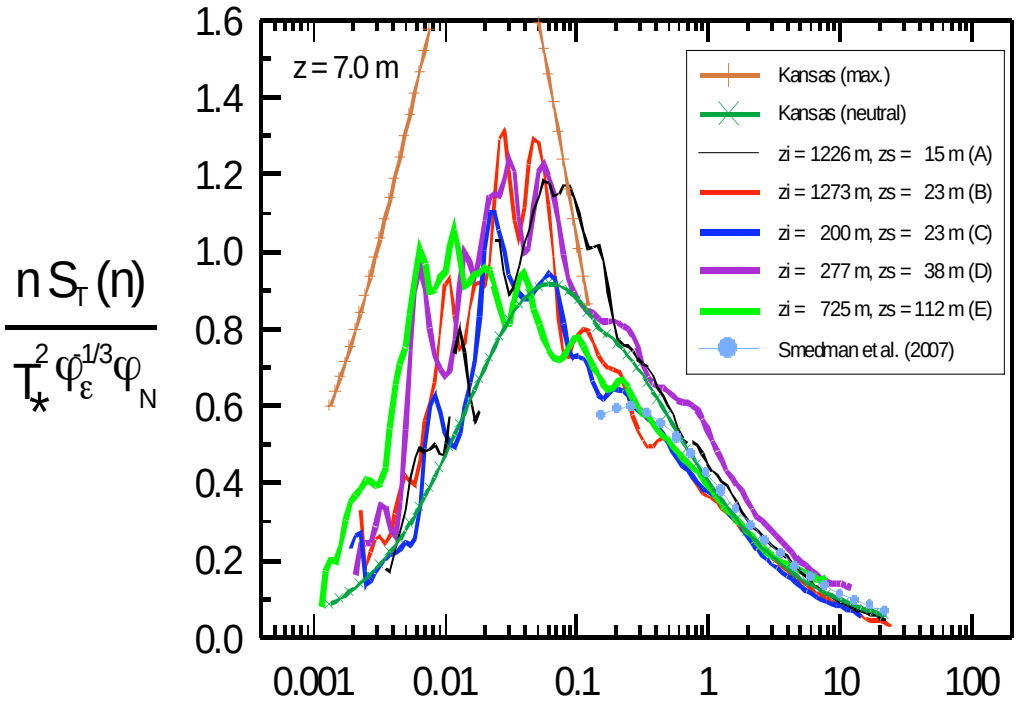

Fig. 4 Temperature spectra for Coorong at 7.0 m height, scaled with stability-dependent factors on the amplitude axis and local wind speed on the frequency axis. The spectra are averaged separately for the five classes defined in Table 2. Also shown are the neutral (0^+) Kansas spectrum, the upper limit of the unstable range found at Kansas (Kaimal et al. 1972), and the "unstable very close to neutral" spectrum of Smedman et al. (2007) for $n\,z/u > 0.15$.

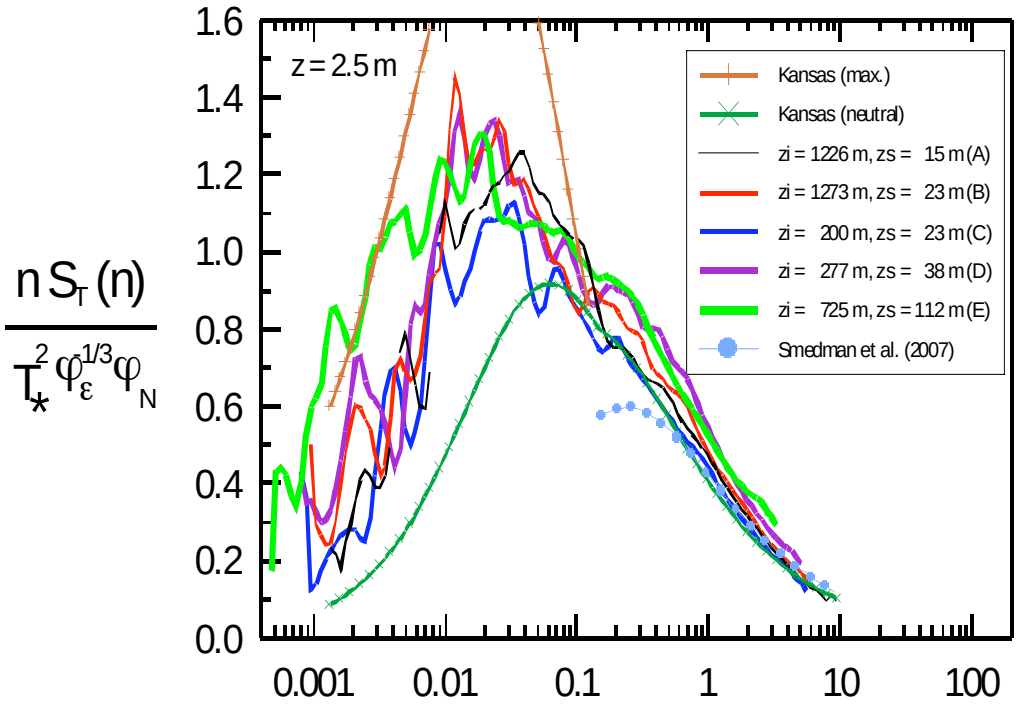

Fig. 5 Same as Fig. 4 but at 2.5 m height.

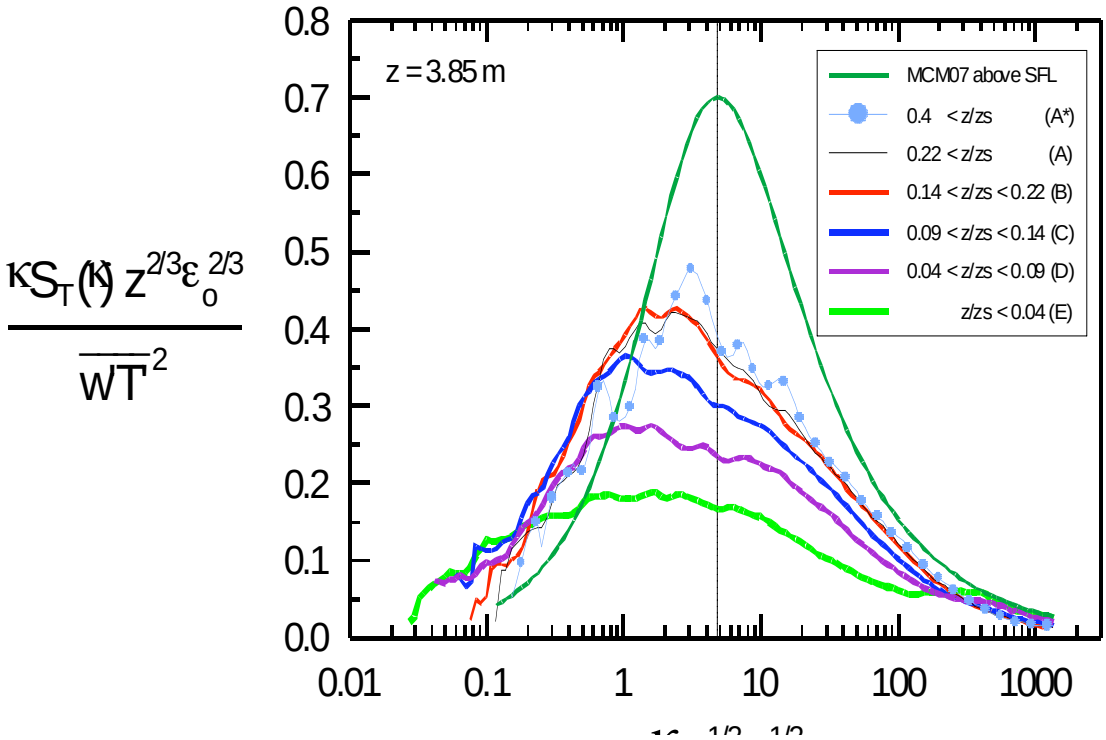

Fig. 6 Temperature spectra for Aorangi, scaled according to the scheme that McNaughton et al. (2007) found valid closely above the SFL. The spectra are averaged separately for the six classes defined in Table 1. The peak wavenumber of the model spectrum above the SFL is marked by a vertical dashed line.

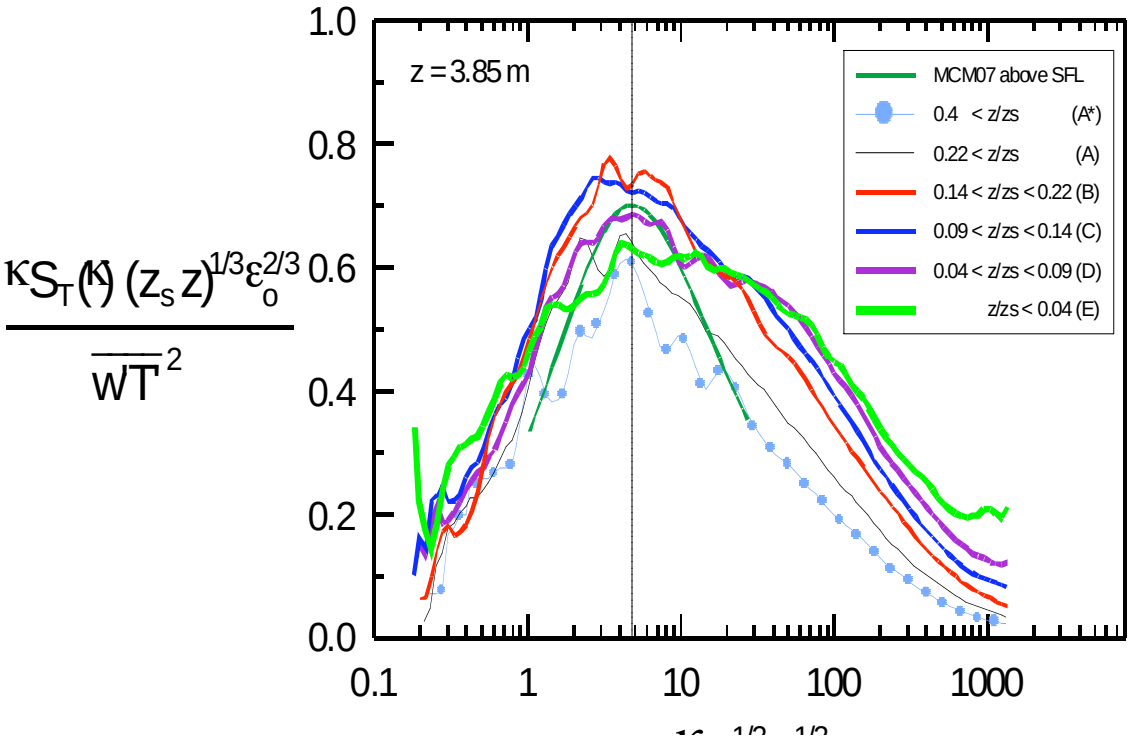

Fig. 7 As Fig. 6 but with mixed length scales including SFL depth on both axes. Also shown is the peak region of the spectrum above the surface friction layer from McNaughton et al. (2007), with z replacing z_s on both axes. The peak wavenumber of the latter is marked by a vertical dashed line.

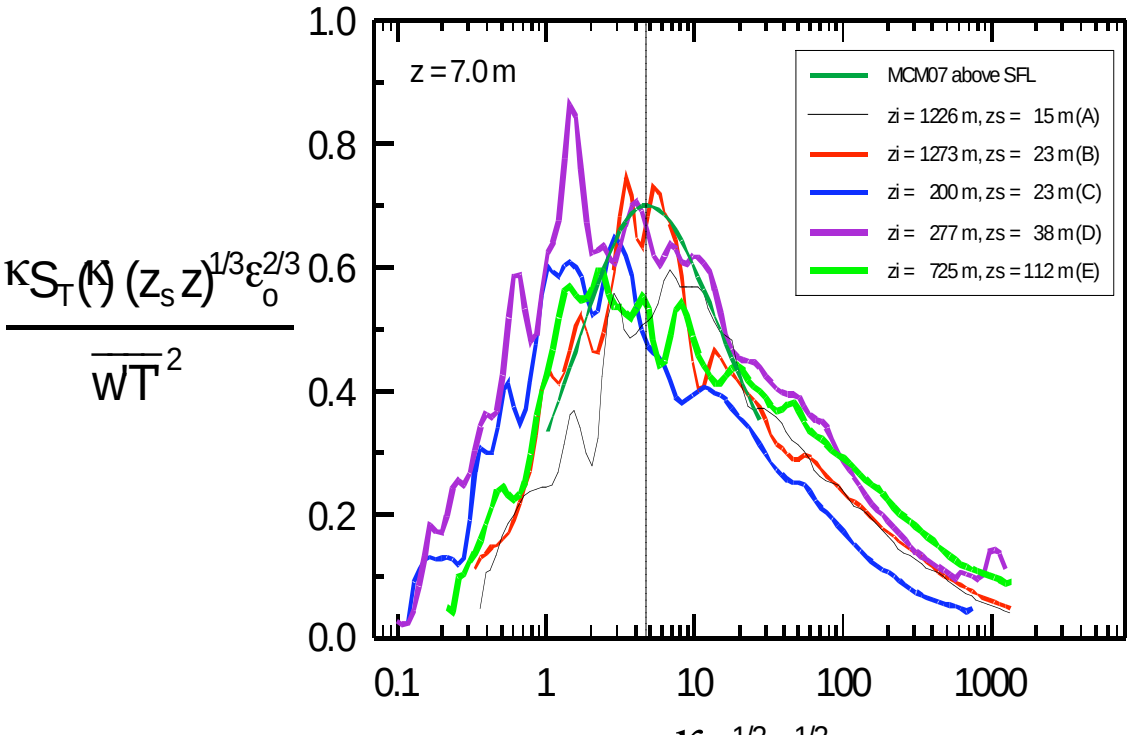

Fig. 8 Temperature spectra for Coorong at 7.0 m height, scaled according to the impinging-eddies model, with mixed length scales including SFL depth on both axes. The spectra are averaged separately for the five classes defined in Table 2. Also shown is the peak region of the spectrum above the surface friction layer from McNaughton et al. (2007), with z replacing z_s on both axes. The peak wavenumber of the latter is marked by a vertical dashed line.

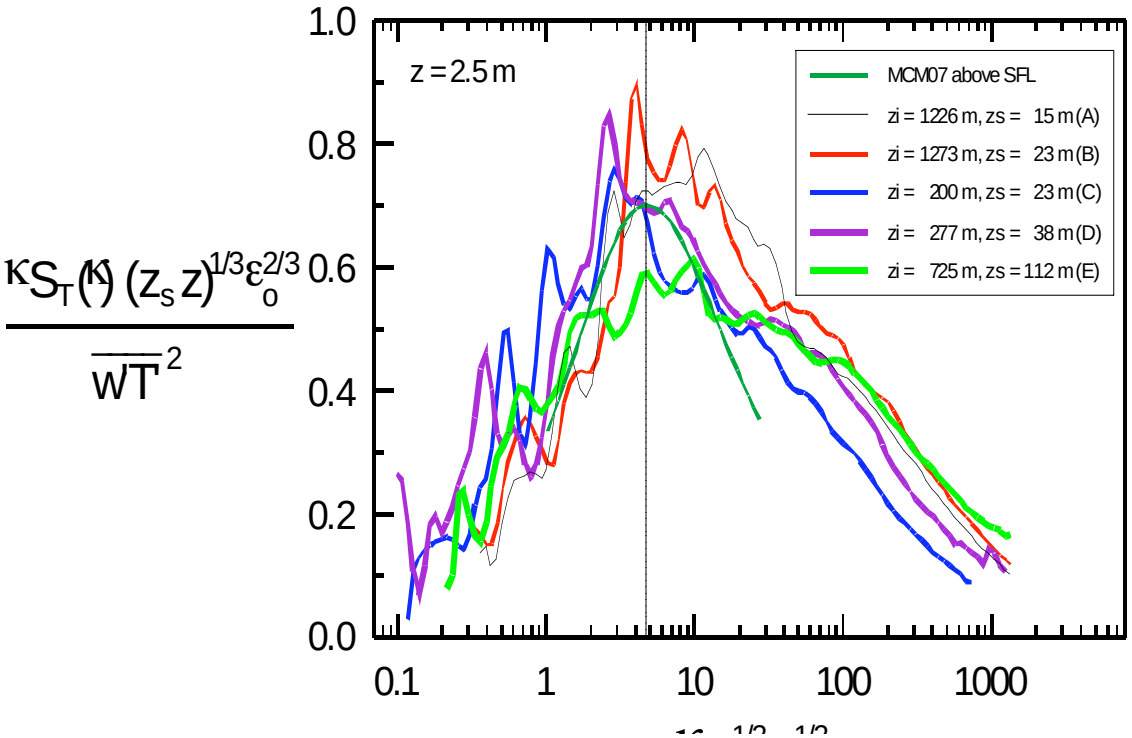

Fig. 9 Same as Fig. 8 but at 2.5 m height.

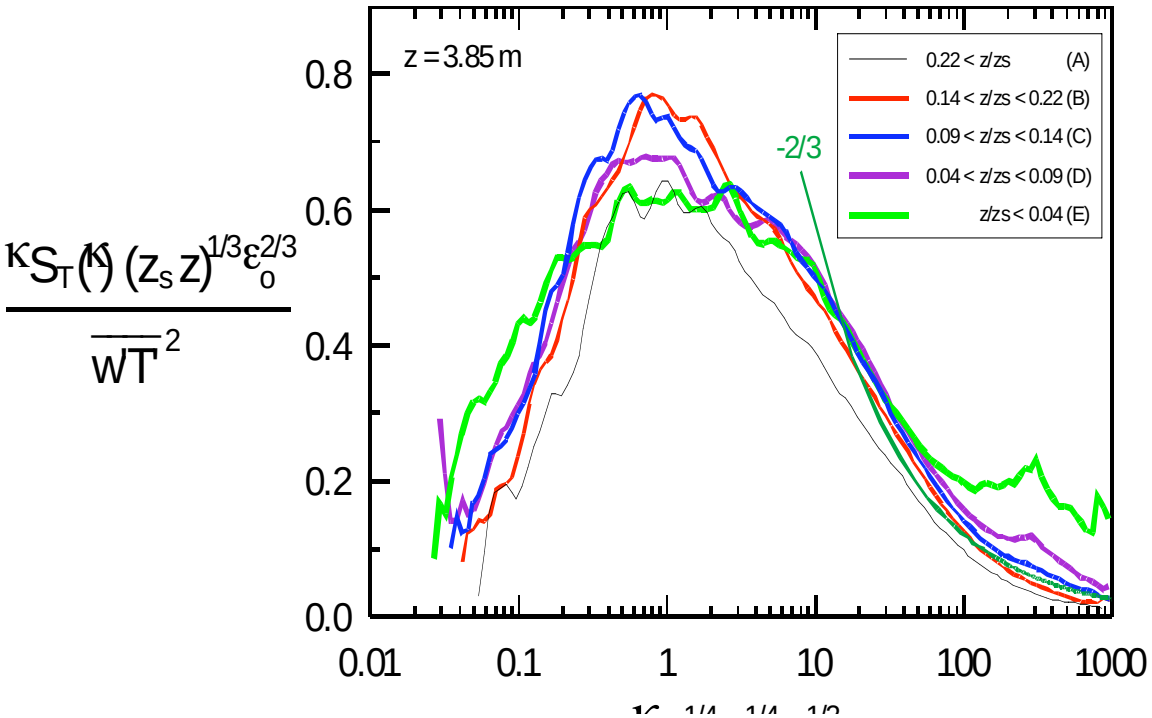

Fig. 10 Temperature spectra for Aorangi, with amplitude scaling as in Fig. 7 and doubly-mixed length scale on the wavenumber axis. The curve labelled "−2/3" describes the function 2.63 $(\kappa\, z_i^{1/4}\, z_s^{1/4}\, z^{1/2})^{-2/3}$.

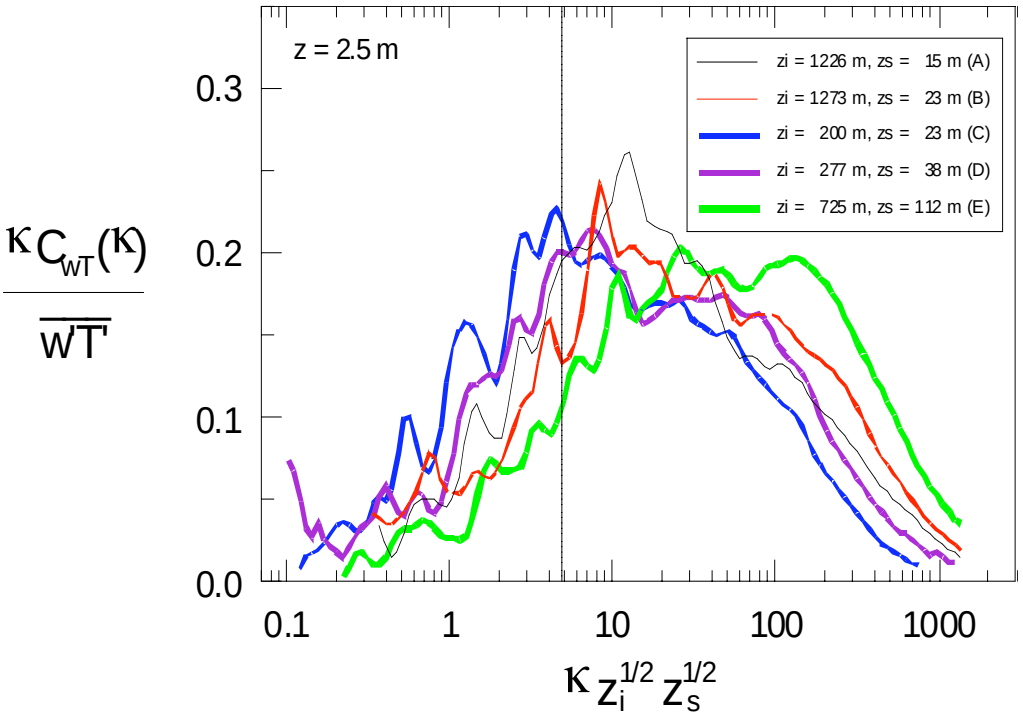

Fig. 11 Heat flux cospectra for Coorong at 2.5 m height, with the same wavenumber scaling as for *T* spectra in Figs. 7 to 9. The peak location of the *T* spectrum above the SFL, from McNaughton et al. (2007), is marked by a vertical dashed line.

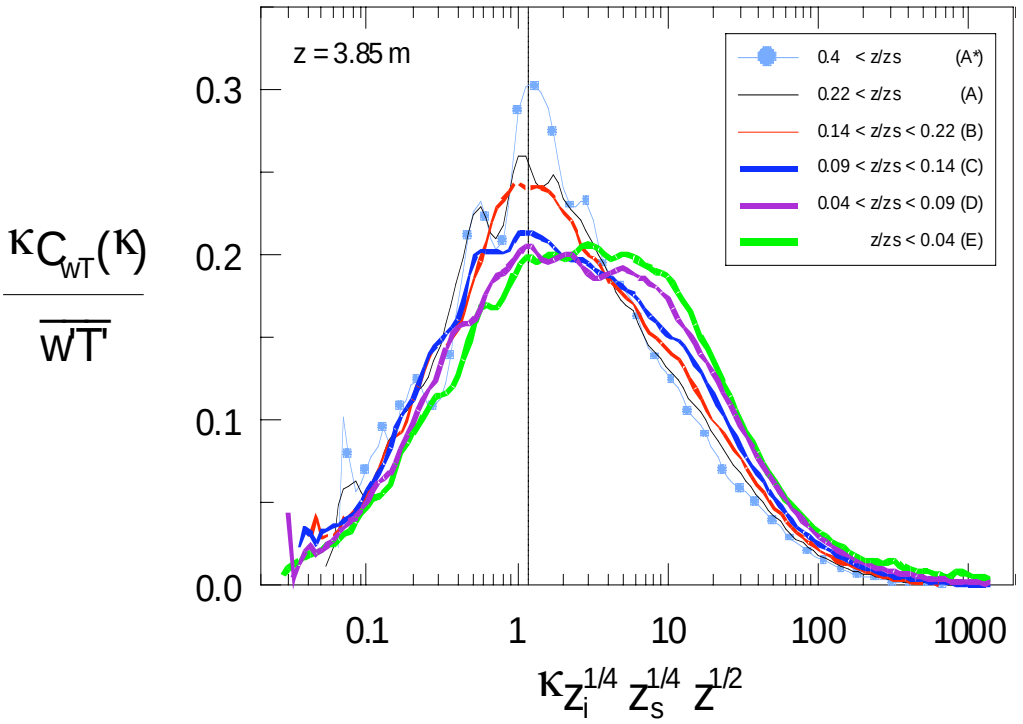

Fig. 12 Heat flux cospectra for Aorangi, with doubly-mixed wavenumber scaling. The average peak location for all classes except E is marked by a vertical dashed line, at a scaled wavenumber of 1.2.

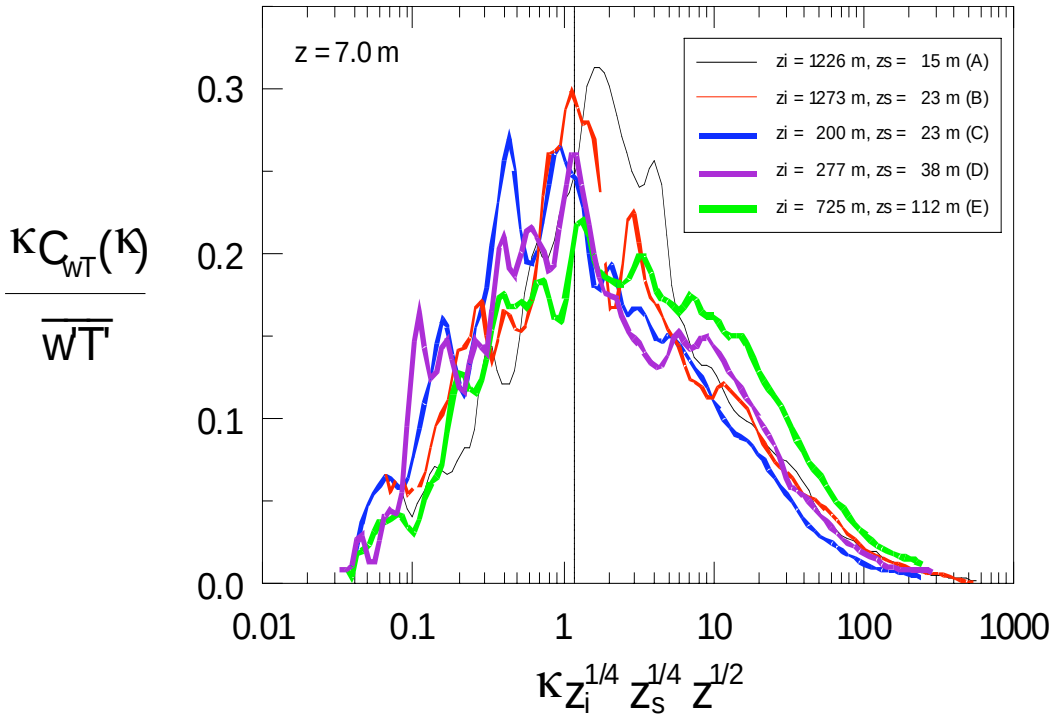

Fig. 13 As Fig. 12, but for Coorong at 7.0 m height.

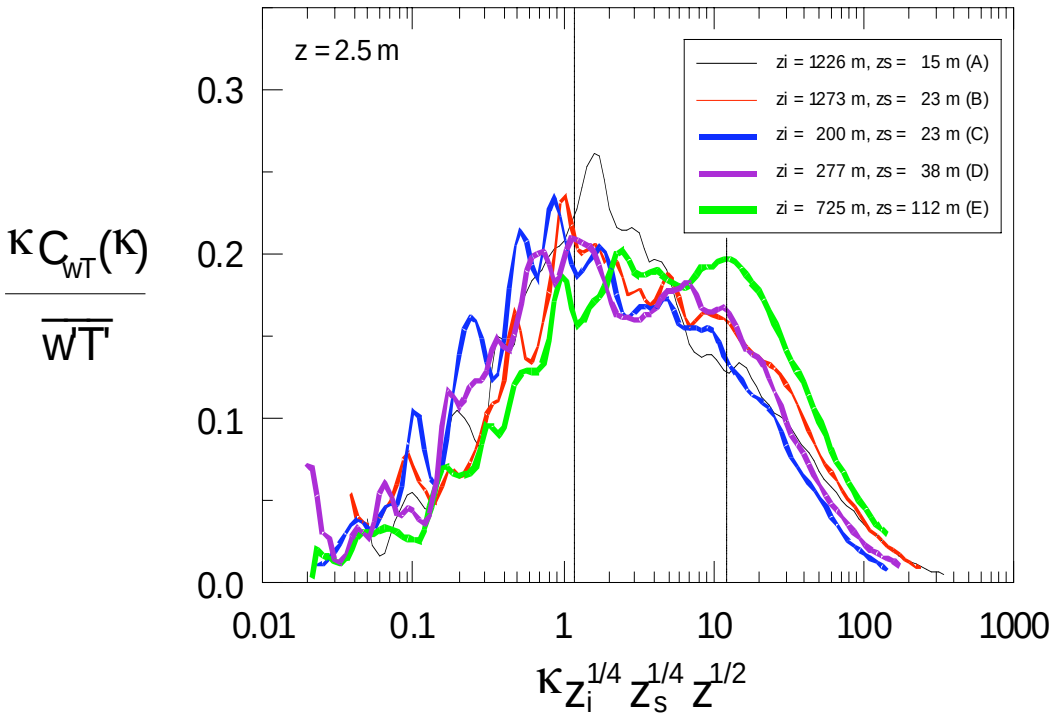

Fig. 14 As Fig. 12, but for Coorong at 2.5 m height. The dotted vertical line indicates the location of the inner-scale peak for Class E, at a scaled wavenumber of 12.

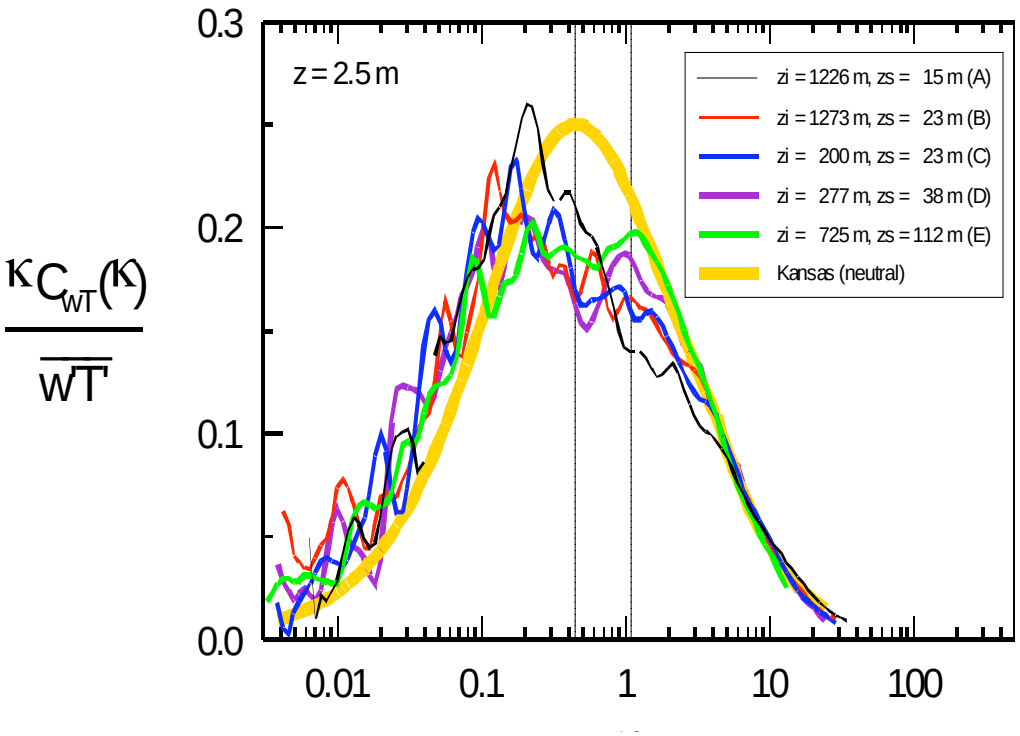

Fig. 15 Heat flux cospectra for Coorong at 2.5 m height, with height above ground as the length scale on the wavenumber axis. Also shown is the neutral (0^+) Kansas cospectrum (Kaimal et al. 1972); its line thickness represents the spread in the u/u_s factor, see text. Vertical dashed line: peak location of the Kansas curve, dotted line: location of the inner-scale peak for Class E, at a scaled wavenumber of 1.1.